nature biomedical engineering

Article

https://doi.org/10.1038/s41551-023-01031-3

Cooperative phagocytosis of solid tumours by macrophages triggers durable anti-tumour responses

Received: 8 December 2021

Accepted: 27 March 2023

Published online: 24 April 2023

Check for updates

Lawrence J. Dooling[1,2,6], Jason C. Andrechak[1,2,3,6], Brandon H. Hayes[1,2,3], Siddhant Kadu[1,2], William Zhang[1,2,3], Ruby Pan[1,2], Manasvita Vashisth[1,2], Jerome Irianto[4], Cory M. Alvey[1,2], Leyuan Ma[3,5] & Dennis E. Discher[1,2,3]

In solid tumours, the abundance of macrophages is typically associated with a poor prognosis. However, macrophage clusters in tumour-cell nests have been associated with survival in some tumour types. Here, by using tumour organoids comprising macrophages and cancer cells opsonized via a monoclonal antibody, we show that highly ordered clusters of macrophages cooperatively phagocytose cancer cells to suppress tumour growth. In mice with poorly immunogenic tumours, the systemic delivery of macrophages with signal-regulatory protein alpha (SIRPα) genetically knocked out or else with blockade of the CD47–SIRPα macrophage checkpoint was combined with the monoclonal antibody and subsequently triggered the production of endogenous tumour-opsonizing immunoglobulin G, substantially increased the survival of the animals and helped confer durable protection from tumour re-challenge and metastasis. Maximizing phagocytic potency by increasing macrophage numbers, by tumour-cell opsonization and by disrupting the phagocytic checkpoint CD47–SIRPα may lead to durable anti-tumour responses in solid cancers.

Macrophage engulfment of another cell or microbe helps to maintain tissue homeostasis and potentially provides a first line of immune defence[1,2]. Within a solid tumour, if a macrophage is to physically engulf a cancer cell, then phagocytic forces[3] must exceed the mechanical strength of the cohesion between solid tumour cells[4]. A large imbalance of such cell–cell interactions has long been seen to drive 'phase separation' in mixtures of diverse tissue cell systems[5]. However, immune-cell segregation is understudied. Intriguingly, clusters of macrophages in tumour-cell nests have been correlated with patient survival for at least two solid tumour types[6,7]. Furthermore, macrophage aggregation in the contexts of tissue injury has been compared to platelet clots that contract collectively to close wounds[8], and macrophage aggregation and fusion is widely reported for foreign body giant cell formation in response to implants and also in osteoclast degradation of bone. On the other hand, tumour-associated macrophages more typically correlate with poor clinical prognoses[9], and such macrophages not only promote growth and invasion in some cancers[10] but also often lack phagocytic function[11].

Phagocytosis of 'self' cells is generally inhibited by a key macrophage checkpoint interaction between signal-regulatory protein alpha (SIRPα) on the macrophage and CD47 on all cells including cancer cells[11–13]. Tumour-cell engulfment can be driven to some extent by anti-tumour monoclonal antibodies (mAbs) that bind Fc receptors on macrophages[14], with anti-CD20 in lymphoma being the clearest

[1]Molecular and Cell Biophysics Lab, University of Pennsylvania, Philadelphia, PA, USA. [2]Physical Sciences-Oncology Center at Penn, University of Pennsylvania, Philadelphia, PA, USA. [3]Bioengineering Graduate Group, University of Pennsylvania, Philadelphia, PA, USA. [4]Department of Biomedical Sciences, College of Medicine, Florida State University, Tallahassee, FL, USA. [5]Pathology and Laboratory Medicine, Perelman School of Medicine, University of Pennsylvania, Philadelphia, PA, USA. [6]These authors contributed equally: Lawrence J. Dooling, Jason C. Andrechak.
e-mail: discher@seas.upenn.edu

example so far where additional patients benefit when the mAb is combined with antibody-based blockade of CD47 (ref. 15). However, similar combinations in solid tumours have considerably lower response rates[16,17]. Understanding of biophysical factors that influence phagocytosis in solid tumours is lacking, despite many phagocytosis pathways being well studied with macrophages attached to a culture dish[1,18,19]. In this Article, we hypothesized that a high number of maximally phagocytic macrophages could work together as a cluster to overcome the cohesive forces and dominate the growth of solid tumours.

Major challenges for macrophage checkpoint blockade in solid tumours include low permeation of anti-CD47 (ref. 20) relative to the potency of inhibitory signalling[21,22] as well as on-target, off-tumour binding of antibodies to ubiquitously expressed CD47. Engineered macrophages that traffic into tumours could conceivably overcome both challenges to improve efficacy and safety of checkpoint blockade, especially if dosing maximizes the number of phagocytic macrophages and any collective or cooperative functions that counter solid tumours and their cohesiveness. Unknown is whether macrophages that certainly constitute a first line of innate immune defence in vivo could also contribute to any form of acquired immunity against cancer[23,24]. Our second main hypothesis is that tumour elimination leads to de novo anti-cancer immunoglobulin G (IgG) with pro-phagocytic function. Such antibodies could complement the tumour-opsonizing mAbs that initiate therapy and can potentially identify new tumour-specific epitopes that can help overcome resistance. Our results with deep macrophage checkpoint blockade indeed provide evidence for cooperative phagocytosis and the elimination of solid tumours as well as for immune memory, including cancer-opsonizing IgGs driving macrophage clustering.

Results

Macrophages cluster when eradicating tumouroids

To determine the requirements for macrophages to eliminate a proliferating, cohesive mass of cancer cells, we engineered 'tumouroids' of B16 mouse melanoma cells in non-adhesive culture plates (Fig. 1a). B16 melanoma is a widely used tumour model for cancer immunotherapy development and does not respond in vivo to T-cell checkpoint blockade nor to CD47 disruption[25]. This particular tumour model therefore represents a large number of patients thus far unresponsive to immunotherapy[26]. Moreover, because monotherapy with CD47 blockade shows no clinical efficacy against solid tumours[16], it was important to focus on a cancer line such as B16 that is anticipated to be similarly unaffected by CD47 disruption, rather than study lines that respond to CD47 disruption alone (for example, MC38 colon cancer[27,28]). B16 tumouroid cells adhere to each other and grow as thin, dark cell aggregates with irregular borders (Extended Data Fig. 1a), akin to early-stage melanoma in the upper layer of human skin[29]. Tumouroids resist deformation as a single cohesive mass when pulled into a micropipette (Fig. 1b), with a softness consistent with other neuro-lineage tissues such as brain that also relies for cohesion more on cell–cell adhesion than matrix adhesion[30]. Sustainable stresses of ~0.5–1 kPa are much higher than those exerted by a macrophage engulfing a microparticle[3], but tumouroids flow after a few minutes as the stress favours disruption of adhesions. Such observations illustrate a means by which added macrophages can over time extract B16s from the tumouroid. Viscoelastic behaviour is typical of culture-aggregated spheroids, including cell mixtures that sort on the basis of differential adhesion and cortical tension[31,32]. Indeed, disrupting either Ca^{2+}-dependent cell adhesions or actin polymerization relaxed tumouroids as evidenced by a rapid (<1 h) increase in projected area (Extended Data Fig. 1b–d). Subcutaneous tumours of B16s from mice exhibit similar cohesion and softness (Extended Data Fig. 1e–h), despite the presence of various other cell types, including macrophages.

We hypothesized that cancer phagocytosis could be maximized for targets lacking CD47, and we therefore generated tumouroids from clustered regularly interspaced short palindromic repeats (CRISPR)/Cas9-engineered B16 cells with either *Cd47* knockout (KO) or wild-type (WT) levels of CD47 (Extended Data Fig. 2a). Bone marrow-derived macrophages (BMDMs) were added to pre-assembled tumouroids together with anti-Tyrp1 mAb that binds and opsonizes B16 cells (Extended Data Fig. 2a,b). Tyrp1 aids in melanin granule synthesis, so that anti-Tyrp1 is relatively specific to melanocytes in contrast to the ubiquitous phagocytosis checkpoint ligand CD47 (Extended Data Fig. 2c). Despite the specificity, anti-Tyrp1 was recently found ineffective in the clinic against melanoma[33] and shows little to no effect on B16 tumours established in mice[25]. Growth of WT tumouroids is likewise unaffected by anti-Tyrp1 with or without added macrophages, but we do find that opsonization of CD47 KO 'immuno-tumouroids' maximizes phagocytic macrophages quantified ~1 day after addition (Fig. 1c and Supplementary Fig. 1). Conventional assays with cancer cell suspensions added to immobilized macrophages for 1–2 h show similar phagocytosis trends (Extended Data Fig. 2d), and despite an important difference elaborated below, the results all suggest that macrophages in tumouroids can extract and engulf individual B16s, as clearly visualized for opsonized CD47 KO tumouroids (Fig. 1d(i)). More than 80% of engulfment events showed co-localization of green fluorescent protein (GFP) and DNA, which we considered to represent phagocytosis of an entire cell including its nucleus and cytoplasm. A minority of engulfment events did not stain positively for DNA and might instead represent trogocytosis of cytoplasmic fragments, which will depend on macrophage-to-target ratios and could conceivably contribute to tumour cell elimination[34,35] along with other forms of cell death (Extended Data Fig. 2e). Importantly, only for the maximal phagocytosis condition of CD47 KO and anti-Tyrp1 opsonization is the exponential growth of tumouroids reversed and tumouroids eradicated (Fig. 1d(ii) and Extended Data Fig. 3a).

Macrophages cooperatively phagocytose targets

Surprisingly, macrophages segregate under maximal phagocytosis conditions (Fig. 1d(i)). Compared with dispersed macrophages, such a cluster will have relatively few macrophages next to cancer cells and will physically impede interactions with cancer cells. Despite the macrophage clustering, adding more macrophages suppresses growth and fits the calculus of cell proliferation suppressed on a stoichiometric basis by n phagocytes that form a cooperative unit within the cluster (Fig. 1e and Extended Data Fig. 3b). The rate constant k_{eff} exhibits a Hill slope $n = -2.2$ for CD47 KO tumouroids that indicates cooperative phagocytosis by n macrophages as a function of effector-to-target ratio (that is, macrophage:B16) (Supplementary Fig. 2a,b). WT tumouroids could be eliminated by high concentrations of anti-CD47 and anti-Tyrp1 plus high macrophage numbers, and tumouroid area again indicated cooperativity as a function of added macrophages but not as a function of anti-CD47 or anti-Tyrp1 (Fig. 1f,g, Extended Data Fig. 3c–f and Supplementary Fig. 2c–e). High-dose anti-CD47 blockade can be difficult to achieve clinically given the low permeation of solid tumours[4], but high-dose opsonization does not seem to be required for tumouroid elimination provided that CD47 signalling is completely disrupted by genetic KO in target cells as shown here or using engineered macrophages discussed below. The results also underscore a cell-level cooperativity that reflects a cell-level structure such as a macrophage cluster. Indeed, although CD47 KO or anti-CD47 plus anti-Tyrp1 enhanced engulfment of B16 suspensions in standard 2D phagocytosis assays relative to controls, the phagocytic index was weakly anti-correlated with macrophage density (Extended Data Fig. 3g,h)—contrary to cooperativity—and engulfment increased linearly with macrophage density until saturating target cells (Extended Data Fig. 3h and Supplementary Fig. 2f). Tumouroid cohesion might be needed for macrophage cooperativity, with macrophage clusters providing a structural basis for this functional cooperativity—in a hypothetical 'tug-of-war' on

https://doi.org/10.1038/s41551-023-01031-3

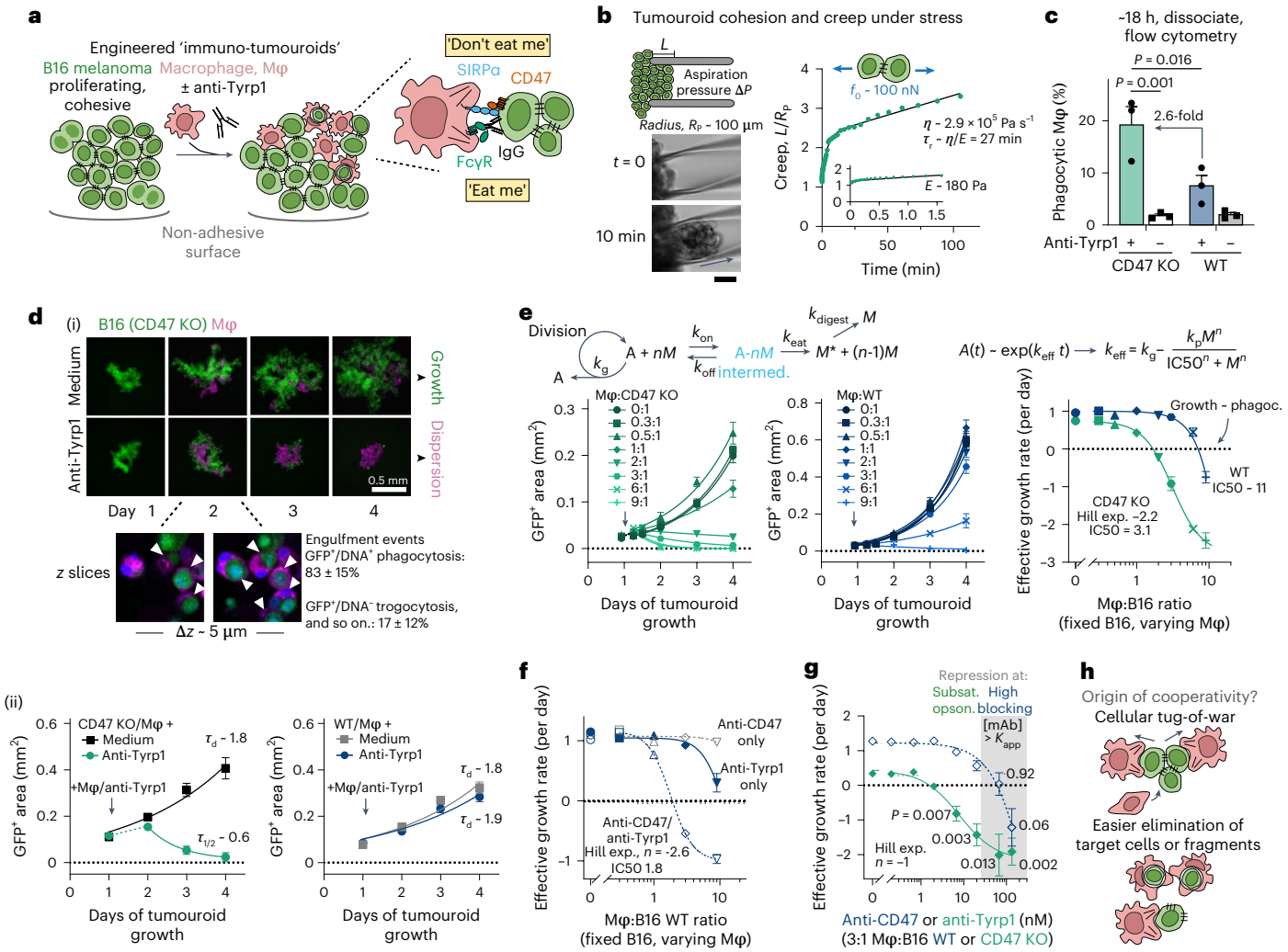

Fig. 1 | Macrophages cooperatively phagocytose IgG-opsonized cancer cells in engineered tumouroids. a, Engineered 'immuno-tumouroid' model comprising cohesive cancer cells (B16 melanoma on non-adhesive surfaces), BMDMs and opsonizing anti-Tyrp1 IgG antibody (Ab). The inset depicts a macrophage-tumouroid 'phagocytic synapse' with FcR–IgG signalling that promotes phagocytosis and CD47–SIRPα that inhibits phagocytosis. **b**, Micropipette aspiration of B16 tumouroids with representative brightfield images at $t = 0$ and 10 min of constant aspiration pressure, ΔP. Scale bar, 50 μm. Tumouroid creep (L/R_P, where L is the extension into the pipette and R_P is the pipette radius) plotted versus time. The solid line is non-linear regression to the standard linear model to determine the elastic modulus (E) and viscosity (η). Inset: first 90 s of the creep experiment. Forces on the order of 100 nN are predicted to be sustained by tumouroids without rupture based on typical aspiration pressures. **c**, Phagocytosis of CD47 KO and WT B16 tumouroids. The percentage of phagocytic macrophages corresponds to GFP$^+$ macrophages in disaggregated tumouroid cell suspensions ~18 h after addition of macrophages (mean ± standard error of the mean (s.e.m.), $n = 3$ where each replicate consists of cells pooled from the same 96-well plate). Statistical significance was assessed by two-way analysis of variance (ANOVA) and Tukey's multiple comparisons test. **d**, Representative fluorescence images (**d**, i) depicting growth or repression of CD47 KO (green) in immuno-tumouroids from days 1 to 4 when untreated (top row) or treated with anti-Tyrp1 (bottom row). Macrophages (magenta, ~1:1 ratio to initial B16 number) and anti-Tyrp1 were added immediately after the day 1 images were acquired. Scale bar, 0.5 mm. Inset: confocal z slices of CD47 KO immuno-tumouroids depicting B16s engulfed by macrophages (white arrows). Engulfment events were considered cellular phagocytosis when the internalized GFP signal colocalized with DNA signal from an internalized nucleus (mean ± standard deviation (s.d.), $n = 3$ tumouroids). Tumouroid growth (**d**, ii) was measured by quantifying the projected GFP$^+$ area at indicated timepoints (mean ± s.e.m., $n = 6$ tumouroids for WT+ anti-Tyrp1 and 5 tumouroids for other conditions). Solid lines are non-linear regression of the data to the exponential $A(t) = A_1 e^{k(t-1)}$. **e**, A reaction-kinetic model accounts for division of cancer cells (A) in tumouroids and phagocytosis by n macrophages (M). Growth curves (left) for CD47 KO and WT tumouroids with varying ratios of macrophages:B16 fit as in **d** (mean ± s.e.m., $n = 8$ tumouroids per condition, representative of five experiments). Effective growth rate (k_{eff}) plotted against the macrophage:B16 ratio (right). The solid lines are non-linear regression of k_{eff} to the Hill-like equation shown above the plot. **f**, Effective growth rates of WT tumouroids with 133 nM anti-CD47 and anti-Tyrp1 as a function of macrophage number (mean ± s.e.m., $n = 7$–8 tumouroids with exact n given in Extended Data Fig. 3c, representative of three experiments). **g**, The effective growth rate of WT tumouroids at a fixed 3:1 macrophage:B16 ratio and 133 nM anti-Tyrp1 as a function of anti-CD47 concentration, and the effective growth rate of CD47 KO tumouroids at a fixed 3:1 macrophage:B16 ratio as a function of anti-Tyrp1 concentration (mean ± s.e.m., $n = 6$–8 tumouroids per concentration with exact n given in Extended Data Fig. 3d,e). Statistical significance was assessed by comparing the mean at each Ab concentration to 0 using the one-sample t-test (two-tailed, reported P values are not corrected for multiple comparisons). The shaded region of the plot approximates concentrations of anti-CD47 or anti-Tyrp1 that exceed the apparent affinity (K_{app}) shown in Extended Data Fig. 2a. **h**, Proposed cooperative tug-of-war by phagocytic macrophages to disrupt target cancer cell adhesions and subsequently phagocytose cells or cell fragments that are no longer attached to neighbours. Hill exp., Hill exponent; intermed., intermediate; subsat. opson., subsaturating opsonizing Ab concentration.

https://doi.org/10.1038/s41551-023-01031-3

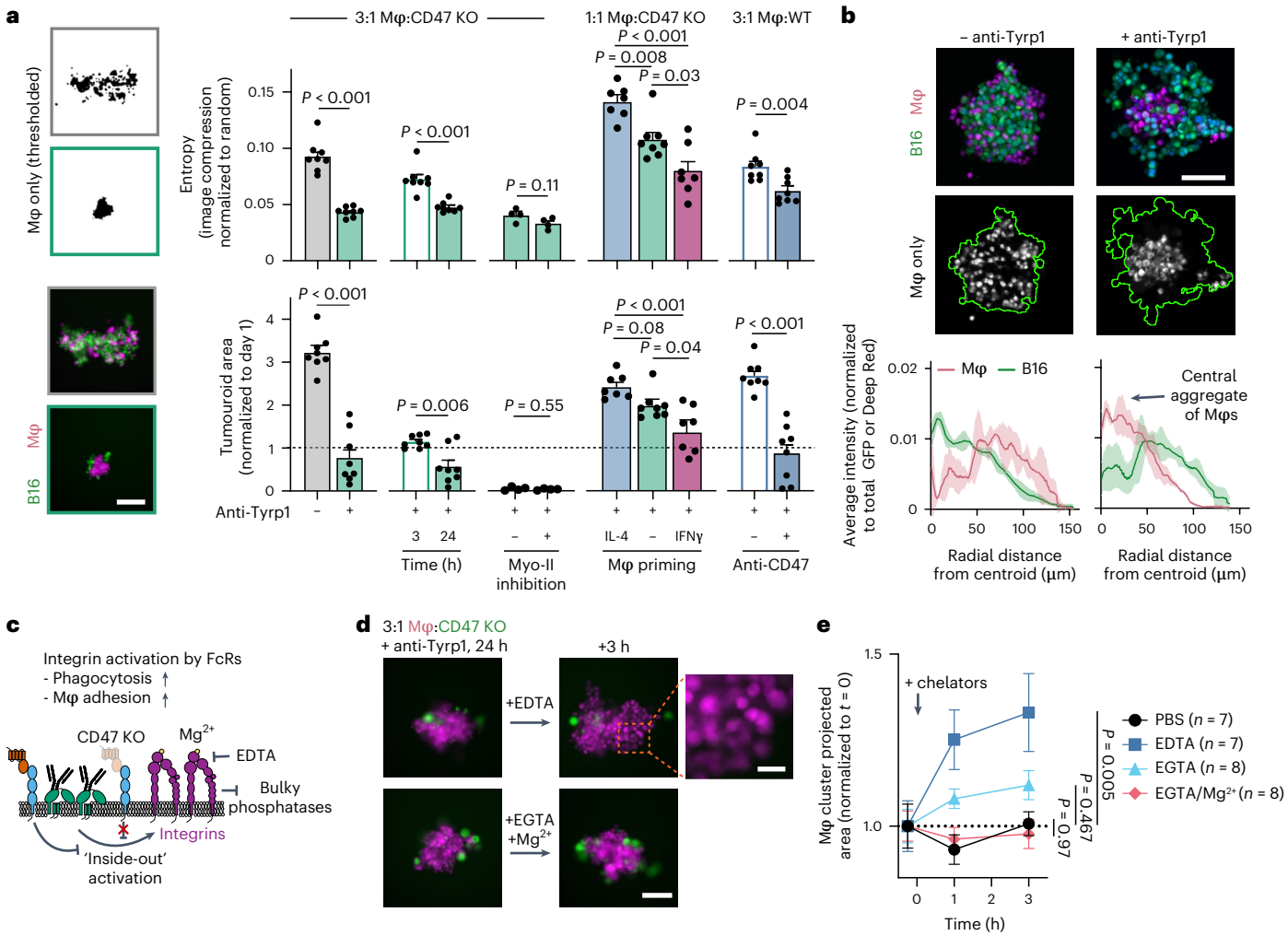

Fig. 2 | Macrophage clusters in tumouroids are consistent with cooperative phagocytosis. a, The informational entropy approximated by image file compression analysis (mean ± s.e.m.) summarizes macrophage clustering within CD47 KO tumouroids across multiple experimental conditions including anti-Tyrp1 opsonization ($n = 8$ tumouroids per condition), kinetic studies ($n = 8$), myosin-II inhibition ($n = 4$) and macrophage priming with IFNγ or IL-4 ($n = 7$ and 8), as well as CD47 antibody blockade on opsonized WT tumouroids ($n = 8$). For details, see Extended Data Fig. 4. Corresponding GFP^+ tumouroid areas (normalized to day 1, mean ± s.e.m.) are shown for the same conditions. Images were acquired ~24 h after addition of macrophages and Abs except in the case of $t = 3$ h tumouroids. Statistical significance was assessed by Welch's t-test (two-tailed, unpaired) for comparisons between two experimental conditions and one-way ANOVA with Tukey's multiple comparisons test for the macrophage-priming experiment with three conditions. The representative thresholded macrophage images (top left) and fluorescence images (bottom left) are from 3:1 macrophage:CD47 KO tumouroids without anti-Tyrp1 (grey frames) and with anti-Tyrp1 (green frames). Scale bar, 200 μm. **b**, Representative maximum intensity projections of confocal fluorescence images (top) of CD47 KO tumouroids 1 day after addition of macrophages with and without anti-Tyrp1. Scale bar, 100 μm. Radial profiles (bottom) of macrophage and B16 fluorescence within CD47 KO tumouroids (mean ± s.d., $n = 3$). **c**–**e**, Disruption of macrophage clusters in tumouroids. Integrin activation (**c**) downstream of Fc receptor signalling when the CD47–SIRPα checkpoint is disrupted potentially enhances phagocytosis and increases macrophage adhesion in tumouroids. Representative images (**d**) of opsonized, CD47 KO tumouroids ~24 h after addition of macrophages and anti-Tyrp1 and 3 h later after addition of chelating agents (2 mM EDTA or EGTA) with or without 5 mM Mg^{2+}. Scale bars, 100 μm (left) and 25 μm (right). The macrophage cluster projected area (**e**) (normalized to $t = 0$) after addition of chelating agents and Mg^{2+} (mean ± s.e.m., tumouroid numbers n given in plot legend, representative of two experiments). Statistical significance at $t = 3$ h was assessed by one-way ANOVA, and adjusted P values were determined by Dunnett's multiple comparisons test between PBS control and other conditions.

cohesive tumouroids by macrophages before successful phagocytosis of target cells (Fig. 1h).

To assess whether macrophage clustering consistently associates with tumouroid suppression, an information entropy approach[36] was applied to our many images obtained under a wide range of timepoints and perturbations. Image files of clustered macrophages are digitally compressed more than images of dispersed (that is, more disordered) macrophages (Fig. 2a and Extended Data Fig. 4a,b), and tumouroid area measurements at the same timepoint show the same trend. Cell density profiles further show a central cluster of macrophages displaces B16 cells in tumouroids only under maximum engulfment conditions (Fig. 2b). Kinetic studies indicate that clustering takes more than 3 h but is clear by 24 h (Fig. 2a). Following tumour cell elimination, macrophages disperse again (Extended Data Fig. 4c,d). Tumouroid elimination and tight macrophage clusters are also promoted by pre-treating cultured macrophages with interferon-γ (IFNγ), which increases phagocytic surface receptors (FcRs) but also induces a low contractility mechanobiological state[11] consistent with soft tumouroid engulfment (for example, Myosin-II inhibition has no effect); interleukin-4 (IL-4) has the opposite effects and disperses macrophages (Fig. 2a and Extended Data Fig. 5a–e). The macrophage priming approach notably avoids direct cytokine effects on B16

growth[37]. Further studies show that macrophage clusters are not sufficient for efficient phagocytosis and tumouroid elimination, but the various analyses do indicate that, when macrophages engulf maximally, they cluster.

Cell–cell adhesion for macrophages is mediated by a diversity of inducible integrins[38,39], with integrin ligand binding for adhesion depending on Mg^{2+} and integrin activation occurring downstream of phagocytic FcR signalling when CD47–SIRPα is inhibited[13]. Consistent with FcR expression increased by IFNγ and decreased by IL-4, monocultures of macrophages cluster with IFNγ and disperse with IL-4 with changes in CD47 and SIRPα levels also suggesting net signalling changes (Extended Data Fig. 5b,e–g). To test the effects of such a pathway on clustering (Fig. 2c), macrophage clusters engulfing CD47 KO cells (~24 h) were treated with chelators (EDTA for Mg^{2+} and Ca^{2+}; EGTA for Ca^{2+}). Only EDTA led to a rapid disaggregation of macrophages (Fig. 2c), which is consistent with the pathway, but EGTA did disrupt B16 aggregates (Extended Data Fig. 1c), consistent with cadherin adhesion.

High doses of phagocytic macrophages can eliminate tumours

To assess whether maximization of phagocytic macrophage dosage is effective in vivo, we first established CD47 KO tumours in mice (for 4 days) and then gave an intravenous (i.v.) injection of anti-Tyrp1 into the tail vein. Just 24 h later, the mAb caused three-fold smaller tumours and three-fold more tumour macrophages ($F4/80^+$ cells) versus controls (Fig. 3a–d). Other immune cells ($CD45^+$ and $F4/80^-$) did not differ. Macrophages also clustered and segregated within treated tumours and circumscribed B16 nuclei and melanin (Fig. 3c,e), consistent with macrophage activation for phagocytosis per tumouroid studies (Fig. 1d and Extended Data Fig. 2f).

Longer-duration experiments showed that anti-Tyrp1 tail-vein injections eliminated CD47 KO tumours in ~40% of mice, whereas various control tumours, including untreated or IgG2a isotype and phosphate-buffered saline (PBS)-treated CD47 KO tumours and both treated or untreated WT tumours all showed the expected exponential growth (Fig. 3f,g and Extended Data Fig. 6a). Partial responders are less frequent with treatment than complete or non-responders (Fig. 3g, inset); assuming that phagocytic macrophage numbers vary broadly in vivo across a cohort, then this bimodal response of tumours in vivo is consistent with the tumouroids in vitro showing cooperative-sigmoidal suppression and elimination (Fig. 1e). The lack of a survival benefit of anti-Tyrp1 on established WT tumours is consistent with recent studies[25]. Previous work established that monocyte-derived macrophages expressing activating FcRs are critical effector cells in subcutaneous B16 tumours treated with anti-Tyrp1 at early timepoints (that is, the day of tumour cell inoculation)[40]. To begin to assess the effect of increased macrophage numbers and any cooperative effects on established CD47 KO tumours, fresh bone marrow cells (containing 5–10% monocytes and macrophages) were intravenously injected together with anti-Tyrp1. The combination eliminated CD47 KO tumours in ~80% of mice (Fig. 3g).

WT tumours are unaffected by i.v. injections of anti-CD47 and anti-Tyrp1 (Fig. 3g), similar to past studies[25], and so we hypothesized that we could eliminate WT tumours by adding i.v. injections of marrow cells engineered most simply by addition of anti-SIRPα to block CD47 interactions (A′PB cells in Fig. 4a). This strategy enabled high levels of phagocytosis and eliminated tumouroids in vitro at high macrophage:B16 ratios (Fig. 4b and Extended Data Fig. 6b). Although this particular anti-SIRPα enhanced phagocytosis of IgG-opsonized red blood cells (RBCs)[41] but had no effect with unopsonized cancer cells[42], it does not directly block CD47 interactions[43] but instead immobilizes SIRPα to prevent its accumulation in the phagocytic synapse[44] (Extended Data Fig. 6d–g). The A′PB approach indeed gave complete responses in ~10% of mice with WT tumours (Extended Data Fig. 6c), which increased to ~17% with anti-CD47 injections and to ~38% with a second i.v. injection of the engineered marrow cells (Fig. 4c). Our recent studies[11] with injection of fluorescent A′PB showed regression of tdTomato-expressing, opsonized tumours in NOD-*scid* $IL2R\gamma^{null}$ (NSG) mice, and A′PB cells in these tumours were activated for phagocytosis on the basis of gene expression and on tdTomato uptake, consistent with images of B16 engulfment here (Fig. 3b).

To confirm macrophages are the key effector cells in vivo and to improve upon transient antibody-based SIRPα blockade with a genetic engineering approach, we deleted SIRPα in conditionally immortalized macrophage (CIM) progenitors that retain macrophage differentiation ability and phenotypes[45,46] (Extended Data Fig. 7a). These engineered macrophages, SIRPα-KO CIM, also readily phagocytosed target B16s with anti-Tyrp1 opsonization in vitro (Fig. 4d). Tail-vein injection of SIRPα-KO CIMs with anti-Tyrp1 (but no added anti-CD47) produced complete anti-tumour responses against WT tumours in ~60% of mice (Fig. 4e). Thus, maximizing phagocytosis favours tumour elimination and high numbers of phagocytic macrophages maximize efficacy (Fig. 4f and Extended Data Fig. 6h).

Macrophages and related phagocytic immune cells provide just a first line of defence but often initiate acquired immunity[23,24]. We therefore challenged surviving mice with a second injection of CD47 KO cells 80 days after the initial challenge and again treated with anti-Tyrp1 (a prime-boost strategy for an anti-cancer vaccine). From the initial cohort in which the complete response rate was about 40% (Fig. 3g), about 80% of the re-challenged mice survived (Fig. 5a). Age-matched naïve mice receiving their first challenge with or without treatment responded similarly to the younger cohorts. A third tumour challenge was left untreated (that is, no anti-Tyrp1), and 75% again resisted tumour growth, which indicates a durable immunological memory. Whitening of the melanized fur was evident across all three challenges of treated mice in the KO cohorts, consistent with an immune response against normal melanocytes that occurs over time with anti-Tyrp1 as mediated by Fc or complement receptors[47]. A second model of B16s involving metastasis to lung with CD47 KO cells showed that anti-Tyrp1 prolongs survival of naïve mice until all mice succumb with clinical symptoms (Fig. 5b). Importantly, however, mice that previously showed complete responses against subcutaneous tumours could achieve a complete anti-tumour response against lung metastasis when treated with anti-Tyrp1, as demonstrated by long-term survival of ~35% of mice.

Although the increased survival rates with engineered macrophages indicate that these are key effector cells, we assessed tumour growth in NSG mice that lack all adaptive immunity (no antibodies and no T cells, B cells or NK cells) but have macrophages that display suitable Fc receptors[11]. Growth of CD47 KO B16 tumours proves similar in NSG mice to growth in C57 mice, and anti-Tyrp1 i.v. injections again slowed the growth of tumours in NSG mice by up to 50% (Fig. 5c). WT B16 tumours are similarly suppressed by SIRPα-KO CIM treatments (Fig. 5d). Such results underscore the key initiating role of macrophages as effector cells in the B16 tumour suppression.

Convalescent serum IgG drives tumour phagocytosis and macrophage clustering

Despite the importance of anti-Tyrp1 for tumour elimination in immunocompetent C57, this mAb was not used in a third challenge of CD47 KO tumours cells in which 75% of mice resisted the tumour (Fig. 5a). We hypothesized therefore that an acquired immune response is generated that might also extend beyond Tyrp1. We thus knocked out Tyrp1 in the CD47 KO cells (double knockout, DKO) and engrafted these DKO cells in complete responders from the initial CD47 KO treatment cohort. We found that, without monoclonal anti-Tyrp1 treatment, which would not be effective against DKO tumours anyway, 50% of mice survived (Fig. 5e).

Serum collected throughout tumour challenge and treatment experiments was used to immunoblot B16 lysates, which revealed an increasing number of bands with progression of challenges in support of our hypothesis of immune responses against B16 antigens beyond

https://doi.org/10.1038/s41551-023-01031-3

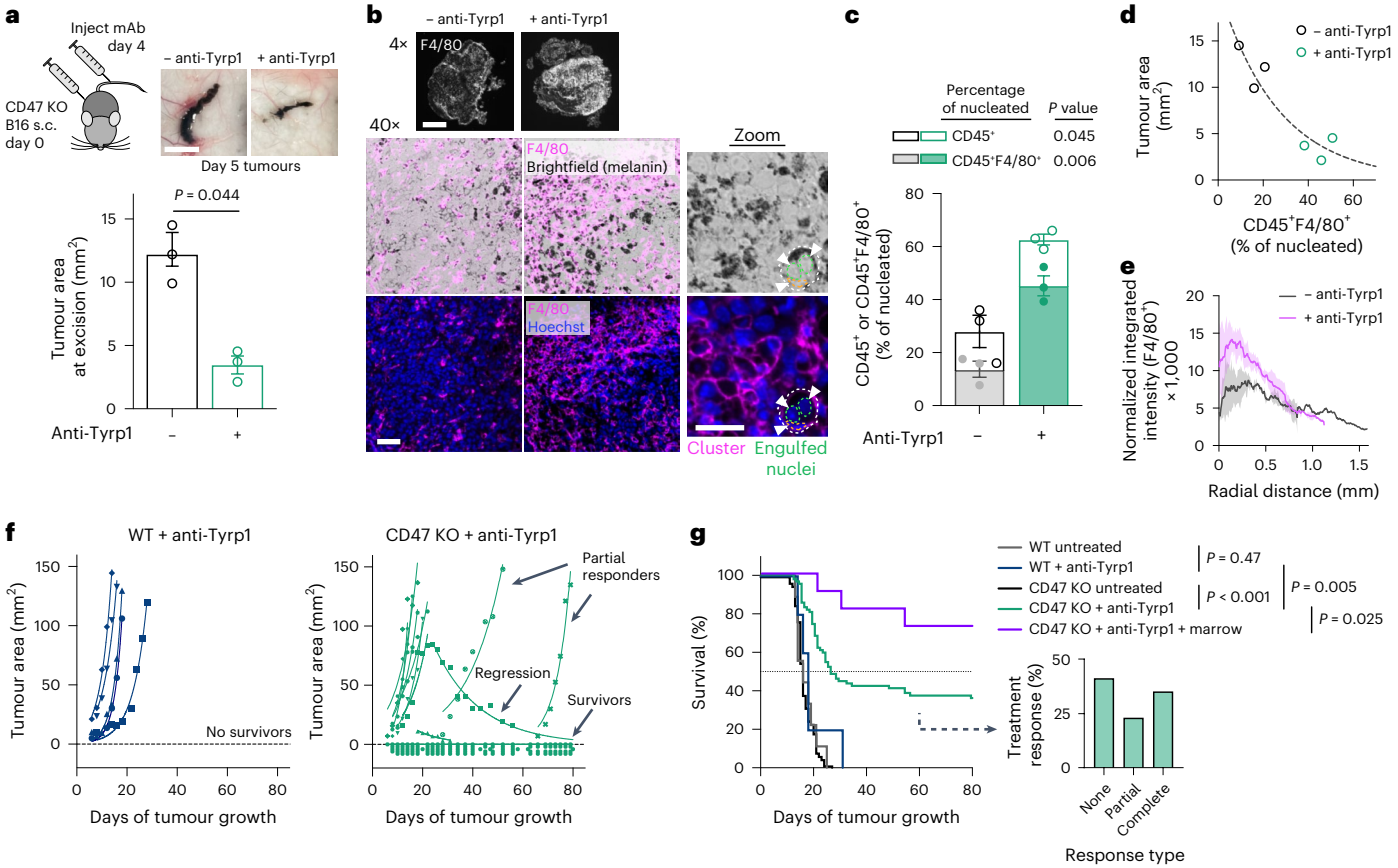

Fig. 3 | Macrophages infiltrate, cluster and repress CD47-depleted syngeneic tumours in vivo only in combination with therapeutic IgG opsonization. **a**–**e**, Analysis of tumour size and immune infiltrate following treatment with anti-Tyrp1. Tumours were isolated on day 5 after subcutaneous (s.c.) injection of 2×10^5 CD47 KO cells. Treated mice had received a single dose of 250 µg anti-Tyrp1 on day 4. Representative photographs (**a**) of CD47 KO tumours in dissected mice that had received anti-Tyrp1 treatment or were left untreated. Scale bar, 1 mm. Tumour area was measured from photographs (mean ± s.e.m., $n = 3$ mice per group). Statistical significance was assessed by Student's t-test (unpaired, two-tailed). Representative fluorescence and brightfield images (**b**) of tumour sections stained for F4/80 (magenta). Arrows denote nuclei within the dashed white border of a macrophage engulfing two B16s (green dashed lines, B16 nuclei; orange dashed line, macrophage nuclei). Scale bars, 0.5 mm (4×), 50 µm (40×) and 25 µm (40× zoom). CD45 and F4/80 staining (**c**) of cells isolated from disaggregated tumours (mean ± s.e.m., $n = 3$ tumours per group). Statistical significance was assessed by Welch's t-test (unpaired, two-tailed) for CD45$^+$ staining and by Student's t-test (unpaired, two-tailed) for F4/80$^+$ staining (P values are not adjusted for multiple comparisons). Relationship between tumour area and F4/80$^+$ macrophage infiltrate (**d**), fit with an exponential curve. Radial profile analysis (**e**) of F4/80$^+$ signal in CD47 KO tumours based on 4× images (mean ± s.d., $n = 3$ treated and 2 untreated tumours). **f**,**g**, Tumour growth and survival analysis of mice injected subcutaneously with 2×10^5 WT or CD47 KO cells and treated intravenously with 250 µg anti-Tyrp1 on days 4, 5, 7, 9, 11, 13 and 15 or left untreated. Representative growth curves (**f**) depict projected tumour area versus days after tumour engraftment. Each symbol represents measurements from a separate tumour, and tumour area is fit with the exponential growth equation $A = A_0 e^{kt}$ (solid lines). Complete anti-tumour responses in which a tumour was never palpable are all depicted with the same symbol (filled circle) and solid lines at $A = 0$ ($n = 15$ CD47 KO tumours across two independent experiments and $n = 5$ WT tumours from one representative experiment). Survival analysis (**g**) of mice with WT tumours (treated $n = 5$, untreated $n = 9$ across 1 and 2 independent experiments, respectively) or CD47 KO tumours (treated $n = 82$ across 10 independent experiments, untreated $n = 60$ across 12 independent experiments). In some experiments, mice with CD47 KO tumours were treated with donor bone marrow injections combined with i.v. anti-Tyrp1 treatment ($n = 11$ across 2 independent experiments). Statistical significance was determined by the log-rank (Mantel–Cox) test. The inset bar graph depicts response types for mice with CD47 KO tumours that were treated with anti-Tyrp1. A partial response was considered survival longer than 1 week beyond the median of the untreated CD47 KO cohort (16 days + 7 days = 23 days) and shorter than 80 days.

Tyrp1 (Fig. 5f and Supplementary Fig. 3). To test whether such serum antibodies are functional to promote phagocytosis, we added serum from various mice to CD47 KO and DKO B16 cells and then added this mixture to macrophages in culture. Most convalescent sera increased phagocytosis relative to naïve serum (Fig. 6a), with similar results for CD47 KO, DKO and WT B16 parental cells as targets for phagocytosis (Extended Data Fig. 7b). As expected, anti-Tyrp1 does not drive phagocytosis of DKO cells, and neither anti-Tyrp1 nor the serum from complete responders has any effect on engulfment of YUMM2.1 melanoma cells that were also derived from mice on the C57 background[48] (Fig. 6a). Convalescent serum antibodies thus target B16-specific antigens beyond Tyrp1 but not antigens expressed by a syngeneic melanoma or xenogeneic antigens present on cultured cell lines (for example, bovine antigens from media containing foetal bovine serum (FBS)). Assays of IgG subclasses confirm the presence of pro-phagocytic IgG2a/c and IgG2b (ref. 49) that bind CD47 KO cells and DKO cells after second and third challenges (Fig. 6b and Supplementary Fig. 4), with other IgG subtypes also detected on CD47 KO and DKO but not YUMM2.1 (Extended Data Fig. 8a,b and Supplementary Fig. 4). Further consistent with a progressive prime-boost vaccination and antigenic spread beyond Tyrp1, survivors of the third B16 challenge (with no monoclonal anti-Tyrp1 injected) showed higher levels of IgG2a/c compared with non-survivors.

Definitive de novo anti-B16 IgGs that bind DKO cells were detected in serum weeks after the first challenge (approximately day 45 in Fig. 6b). Immunocompromised NSG mice do not survive this long

https://doi.org/10.1038/s41551-023-01031-3

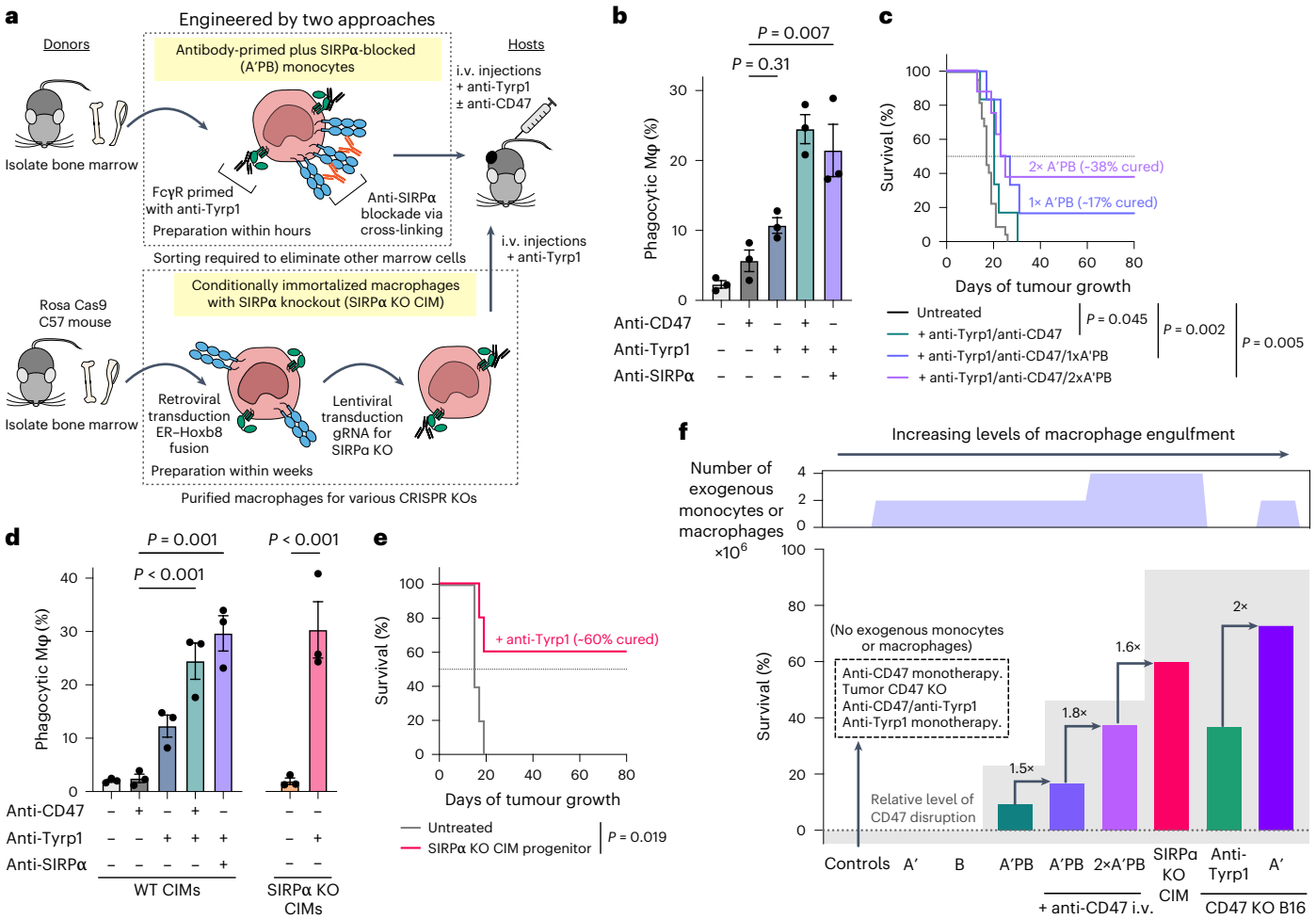

Fig. 4 | Engineered macrophages phagocytose cancer cells efficiently and clear WT tumours in a dose-dependent fashion. a, Two engineered macrophage approaches. Top: A′PB are freshly collected bone marrow cells that are subsequently antibody primed (Fc receptors bound with anti-Tyrp1, A′), Plus (P) SIRPα-blocked (by anti-SIRPα, B). Bottom: CIM progenitors (by oestrogen receptor (ER)-fused Hoxb8) with SIRPα KO as an improvement to anti-SIRPα blockade. To treat tumour-bearing mice, A′PB or SIRPα KO CIM progenitor cells (also Fc-primed with anti-Tyrp1) were injected intravenously on day 4 with subsequent antibody i.v. injections on days 5, 7, 9, 11, 13 and 15. **b**,**c**, Phagocytosis of WT B16 cells by BMDMs and adoptive transfer of antibody-engineered bone marrow cells. In vitro phagocytosis (**b**) of WT B16 by BMDMs with CD47–SIRPα signalling disrupted through anti-CD47 or anti-SIRPα. Statistical significance was assessed by one-way ANOVA with Šídák's multiple comparisons test (mean ± s.e.m., $n = 3$ wells per condition). Survival curves (**c**) of WT (non-KO guide control B16) tumour-bearing mice treated intravenously with anti-CD47 and anti-Tyrp1 combined with either one (1×) or two (2×) doses of A′PB (2×10^7 marrow cells intravenously per dose). The second A′PB dose was administered on day 7. Statistical significance was determined by the log-rank (Mantel–Cox) test (untreated $n = 22$ mice across four independent experiments, anti-Tyrp1/anti-CD47 $n = 6$ in one experiment, anti-Tyrp1/anti-CD47/1x A′PB $n = 6$ in one experiment, anti-Tyrp1/anti-CD47/2x A′PB $n = 8$ in one experiment). **d**,**e**, Phagocytosis of WT B16 cells by differentiated CIMs and adoptive transfer of SIRPα KO CIM progenitors. In vitro phagocytosis (**d**) of WT B16 by unedited (left) or SIRPα KO (right) CIM progenitors that were differentiated to macrophages. Statistical significance was assessed by one-way ANOVA with Sidak's multiple comparisons test (mean ± s.e.m., $n = 3$ wells per condition). Survival curves (**e**) of WT (parental B16) tumour-bearing mice treated with SIRPα KO CIM progenitors as indicated in **a**. Significance was determined by the log-rank (Mantel–Cox) test ($n = 5$ mice per group). **f**, Summary of complete anti-tumour response data across different approaches to maximize phagocytic activity and increase macrophage numbers.

even with injection of SIRPα-KO CIMs (Fig. 5c,d), suggesting that other acquired immune cells (for example, T cells) contribute to survival even before IgG is detectable. Nonetheless, anti-B16 IgG conceivably contribute to acquired immunity by opsonizing tumour cells and by antigen presentation[50] among other effector functions. To test the function of convalescent serum in vivo, CD47 KO B16s were opsonized with the serum just before subcutaneous implantation in naïve mice (Fig. 6c). Tumour growth was suppressed by days 11 and 13 similar to anti-Tyrp1 and relative to controls. However, because any pre-bound IgG will be diluted by B16 proliferation or else lost by dissociation, we assessed complete elimination of tumour cells by convalescent serum and macrophages with tumouroids.

Convalescent serum IgG added with macrophages to CD47 KO tumouroids eliminated tumouroids for the most potent samples (Fig. 6d). Importantly, serum activity against tumouroids correlated with macrophage clustering at day 2 similar to anti-Tyrp1 (Fig. 6d), consistent with effects of monoclonal anti-Tyrp1 (Fig. 2a). Serum alone had no effect (Extended Data Fig. 8c), indicating that macrophages are the effector cells for the anti-B16 serum IgG.

CD47–SIRPα disruption plus IgG opsonization in other immunocompetent tumour models

To begin to generalize some of the findings from our extensive studies with B16, we used the RM-9 prostate cancer model and targeted

https://doi.org/10.1038/s41551-023-01031-3

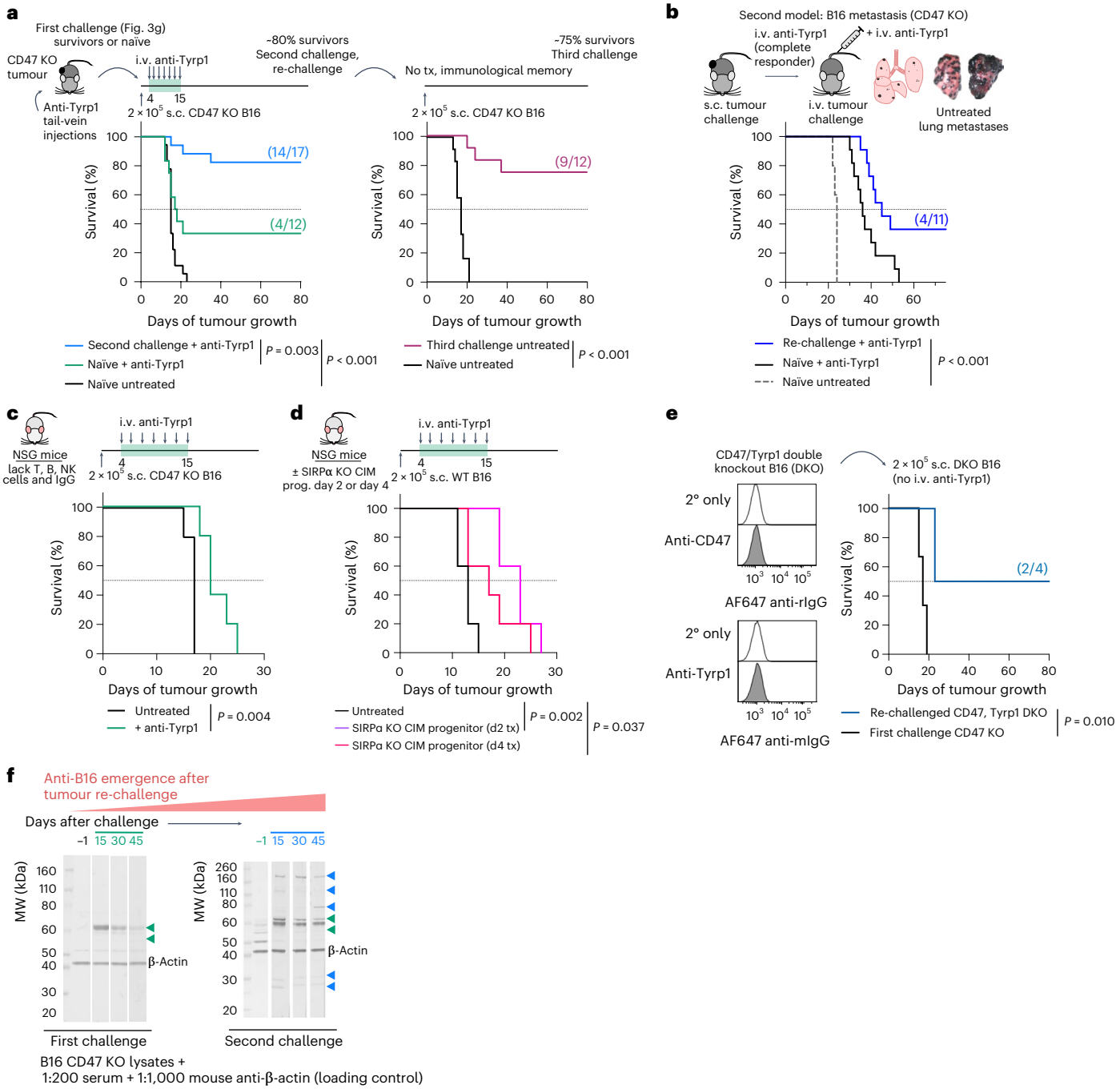

Fig. 5 | Acquired anti-tumour immunity is required for long-term survival and protects against tumour re-challenge, experimental metastases and target antigen loss. a, Left: survival analysis for re-challenge experiments with long-term survivors from Fig. 3g. Mice that survived a first CD47 KO tumour challenge when treated with anti-Tyrp1 were re-challenged with 2×10^5 CD47 KO and treated again with i.v. anti-Tyrp1 ($n = 17$ re-challenges across four independent experiments). As controls, naïve, age-matched mice were challenged and treated a first time ($n = 12$ across three independent experiments) or challenged and left untreated ($n = 18$ across five independent experiments). Right: survival analysis of mice challenged a third time without further treatment (tx) ($n = 12$ re-challenged and $n = 12$ age-matched naïve mice across three independent experiments). **b**, Survival analysis for experimental CD47 KO lung metastases in mice that previously eliminated subcutaneous CD47 KO tumours ($n = 11$ treated with anti-Tyrp1 across two independent experiments) or naïve mice ($n = 11$ treated with anti-Tyrp1 across two independent experiments and $n = 5$ untreated). **c**, Treatment scheme and survival curves of NSG mice engrafted with CD47 KO tumours and treated with i.v. anti-Tyrp1 or left untreated ($n = 5$ mice per group). **d**, Treatment scheme and survival curves of NSG mice engrafted with WT B16 tumours (non-KO guide control) and treated on day 2 or 4 with SIRPα KO CIMs and anti-Tyrp1 intravenously as described in Fig. 4a or left untreated ($n = 5$ per group). **e**, Flow cytometry surface staining of Tyrp1, CD47 KO B16 cells (DKO). 2°, secondary antibody. Survival analysis for DKO re-challenge in mice that were long-term survivors from Fig. 3g ($n = 4$ re-challenged mice and $n = 3$ age-matched naïve mice challenged a first time with CD47 KO). Statistical significance in **a**–**e** was determined by the log-rank (Mantel–Cox) test. **f**, Western blotting of CD47 KO B16 lysate with convalescent serum as primary probe followed by anti-mouse IgG [H+L] secondary staining. Arrows indicate binding of convalescent serum IgG to proteins beyond Tyrp1, which increases in the second tumour challenge. MW, molecular weight. Uncropped blots are shown in Supplementary Fig. 3.

https://doi.org/10.1038/s41551-023-01031-3

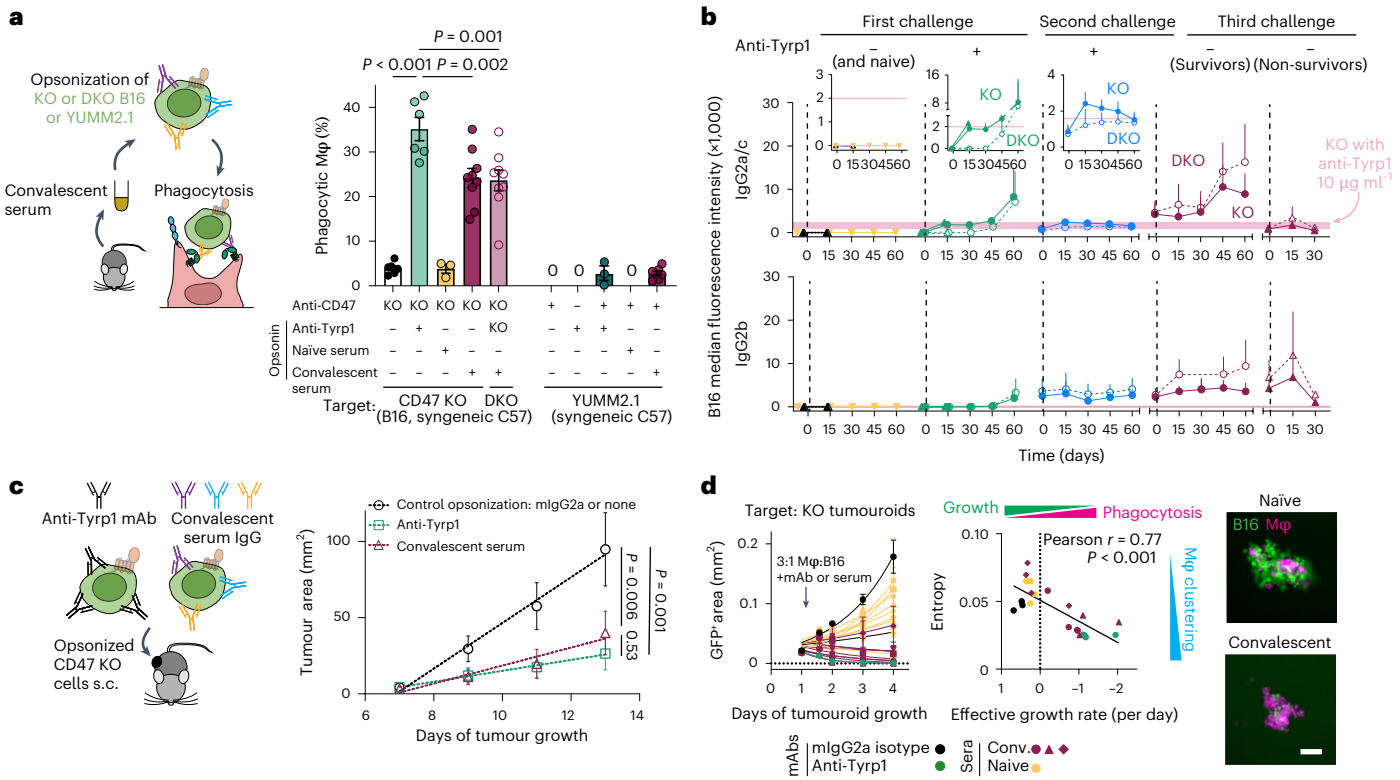

Fig. 6 | Convalescent serum IgG drives B16-specific phagocytosis and clustering in tumouroids, and suppresses tumour initiation in vivo. **a**, Phagocytosis of serum-opsonized CD47 KO B16, DKO B16 or WT YUMM2.1. Statistical significance was assessed by one-way ANOVA with Šídák's multiple comparisons test between selected groups (mean ± s.e.m., anti-Tyrp1 and unopsonized controls: $n = 6$ wells for B16 and $n = 3$ wells for Yumm2.1; serum opsonized: $n = 3$ wells each for 9 convalescent sera and 1 naïve serum). **b**, Kinetic profiles of anti-B16 IgG levels in convalescent sera across the three tumour challenges or in naïve sera. Binding of IgG2a/c and IgG2b to CD47 KO (filled symbols) or DKO (open symbols) was measured by flow cytometry with subclass-specific secondary antibodies and is reported as the median fluorescence intensity (mean ± s.e.m., sera from $n = 4$ survivors, $n = 3$ non-survivors and $n = 5$ naïve). **c**, CD47 KO B16 pre-opsonization with serum or anti-Tyrp1 just before (s.c. flank injection. Tumour area at early timepoints where growth is still in the linear regime (mean ± s.e.m.). Statistical significance was assessed using the extra sum-of-squares F-test (two-tailed, not corrected for multiple comparisons) to compare linear fits (dashed lines) between the pre-opsonized ($n = 5$ mice for convalescent serum and $n = 5$ mice for anti-Tyrp1) and unopsonized ($n = 9$ mice) conditions. **d**, Growth curves and informational entropy of 3:1 macrophage:CD47 KO tumouroids treated with convalescent serum, naïve serum, anti-Tyrp1 or mIgG2a isotype control Ab. Solid lines are non-linear regression of the data to a simple exponential of the form $A(t) = A_1 e^{k(t-1)}$ (mean ± s.e.m., $n = 3$ or 4 tumouroids per sample for 9 convalescent sera, 9 naïve sera and mAbs). Correlation of the informational entropy measured by compression of macrophage image files (acquired ~14 h after addition of macrophages with serum or mAbs) versus the effective growth rate (Pearson $r = 0.77$, $P < 0.001$, two-tailed). For simplicity, data are shown for convalescent sera that produced on average high-entropy (maroon triangles, $n = 3$ tumouroids), medium-entropy (maroon circles, $n = 3$) and low-entropy (maroon diamonds, $n = 4$) macrophage clusters—and low, medium and high growth repression, respectively—and for a representative naïve serum sample (yellow circles, $n = 4$), anti-Tyrp1 (green circles, $n = 3$) and mIgG2a (black circles, $n = 3$). Representative fluorescence images of tumouroids on day 1 after addition of macrophages with naïve or convalescent serum. Scale bar, 100 μm.

the clinically relevant tumour antigen GD2, a ganglioside-lipid on multiple tumour types[51]. Combination of FcR-engaging anti-GD2 mAbs with anti-CD47 recently showed suppression of neuroblastomas and osteosarcomas in immunodeficient NSG mice (with little effect in monotherapies) and also with one syngeneic neuroblastoma in immunodysfunctional 129×1/SvJ mice. In immunocompetent C57 mice, anti-GD2 IgG3, which is ineffective as monotherapy, has been combined with cytokines to suppress RM-9 tumours[24]. The IgG2a anti-GD2 used here strongly promoted engulfment of RM-9 only in combination with anti-CD47, and exponential growth of established RM-9 tumours in C57 mice (which is similar to B16s; Fig. 3a) was suppressed in some mice by tail-vein injections of SIRPα-KO CIMs plus anti-GD2 (Extended Data Fig. 9a). In fully immunocompetent models, this is the first in vivo success with opsonizing anti-GD2 combined with CD47–SIRPα disruption—particularly with an engineered cell therapy.

TC-1 mouse lung cancer cells[52] were also assessed, but a tumour-specific opsonizing mAb is lacking—and a major challenge for many cancers in mice and in the clinic—so we opsonized TC-1 with a polyclonal IgG raised against mouse RBCs that works in RBC phagocytosis[53] and more generally with mouse cells. Pre-opsonization of TC-1 suppressed initial tumour growth in vivo (Extended Data Fig. 9b), analogous to B16 studies (Fig. 6c). Tumour-specific IgG were also sought in C57 mice that survived CT-2A glioma tumours because of vaccine-enhanced CAR-T therapy[54], but serum did not promote phagocytosis even though all murine-IgG subclasses bound to CT-2A (Extended Data Fig. 9c). Binding of Abs far from the cell surface is known to be inefficient in phagocytosis[14]. Anti-cancer IgGs in survivors from a T-cell therapy could thus differ in key functional ways from IgGs induced via phagocytosis in a macrophage therapy.

Discussion

Macrophage immunotherapy of solid tumours benefits from maximizing three factors in combination: first is a high number of phagocytic macrophages, which can lead to cooperativity; second is tumour opsonization, which classically activates Fc receptors for engulfment; and third is deep disruption of the macrophage checkpoint (Fig. 7). Immunocompetent mice that survive develop de novo anti-tumour IgG that are pro-phagocytic and pro-clustering. This might be a first

https://doi.org/10.1038/s41551-023-01031-3

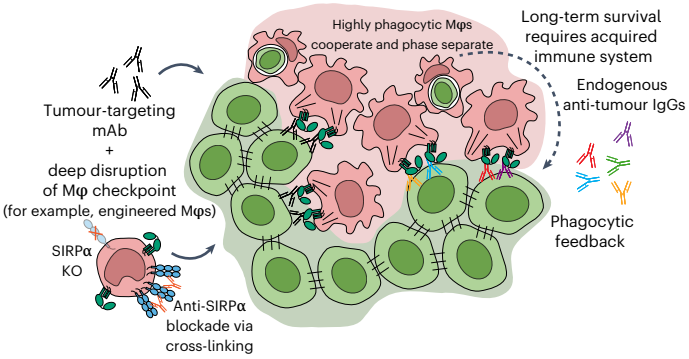

Fig. 7 | Cooperative macrophages eliminate tumour cells to initiate an acquired immune response with phagocytic feedback. Macrophage density and cooperativity combine with IgG opsonization and efficient blockade of the macrophage checkpoint in successful macrophage immunotherapy of solid tumours. Phase-separating macrophages cooperatively engulf cancer cells when CD47 signalling is disrupted deeply and cancer cells are opsonized with IgG to maximize engulfment. Macrophage phagocytosis in tumours treated with anti-tumour IgG mAb initiates an acquired immune response required for long-term survival, which includes the production of de novo endogenous anti-tumour IgGs that are capable of further opsonization for phagocytic feedback.

for tumours, but immunodeficient NOD mice with KO of CD47 can develop anti-RBC IgG and die with anaemia[55], which suggests IgG opsonization of normal host cells and which raises issues of treatment safety. Various effector functions for the anti-cancer IgG are possible in vivo and require further study, but their isolation and cloning (from mouse or eventually patients) could help address a major need for pro-phagocytic IgGs that combine with clinically relevant CD47 blockade for anti-tumour therapy—including resistance with antigen loss. Our approach is thus poised to take advantage of biopharmaceutical expertise in therapeutic mAbs and of new vaccine technologies (such as messenger RNA-based vaccines) to produce tumour-specific IgGs.

The most promising clinical application of CD47–SIRPα blockade so far combines anti-CD47 (magrolimab) and anti-CD20 (rituximab) against the liquid tumour non-Hodgkin's lymphoma[15], but rituximab depletion of B cells prevents the development of anti-tumour IgG and of any phagocytic feedback. Anti-cancer IgG in cancer patients include anti-(human Tyrp1) from a patient with melanoma[56,57], but anti-Tyrp1 lacks clinical efficacy against melanoma[33]. High *TYRP1* in metastatic melanoma associates with poor survival (Extended Data Fig. 10a), suggesting that Tyrp1 is targetable; and although low *CD47* associates with poor survival, even moderate CD47 levels are protective (Fig. 1f). Importantly, engineered macrophages can enhance via their function and their numbers the efficacy of otherwise ineffective Abs. For the many patients with melanoma unresponsive to current therapies, our results specifically suggest that anti-Tyrp1 can be combined with deep CD47–SIRPα disruption and phagocytic macrophages; no such trials are currently registered, and serum could yield new anti-melanoma IgG.

CD47 deletion on its own has no effect on B16 tumours in immunocompetent mice (Fig. 3b). This result aligns well with monotherapy with anti-CD47, which has shown no efficacy in the clinic, particularly against solid tumours[16]. In contrast, some mouse-engrafted tumours show that CD47 monotherapy is efficacious. In particular, one pair of studies has shown that anti-CD47 or CD47 KO[27,28] are effective on their own against liquid and solid tumours (such as MC38 colon tumours) while ruling out any role for macrophages. T-cell depletion abrogated any tumour-growth suppression. Relevance to human patients is now questionable and probably attributable to the high immunogenicity of the tumours. Compared with B16s, many tumour lines (such as MC38) are indeed more immunogenic in immunocompetent mice (Extended Data Fig. 10b). Importantly, RM-9 prostate cells are poorly immunogenic[58] (similar to B16 cells) and show similarly rapid growth (Extended Data Fig. 9a), which anti-correlates with immunogenicity (Extended Data Fig. 10b). Numerous immune cell types and factors probably contribute to the suppression of patient-relevant B16 tumours and could be perturbed or depleted in future studies, including studies of T cells, B cells and especially dendritic cells that are often phagocytic and widely implicated in acquired immunity. Nonetheless, our two approaches with suitably engineered macrophages maximize survival (Fig. 4) even in the absence of any acquired immune cells (Fig. 5d). This indicates a key initiating role for phagocytic macrophages. Such cells accumulate early in tumours and engulf, while the number of other immune cell types ($CD45^+$, $F4/80^-$) remains overall constant (Fig. 2c).

Tumour-associated macrophages are generally not phagocytic[59] but are often abundant, and are associated with a poor prognosis in human tumours such as melanoma[60]. However, phagocytic macrophage clusters in thyroid cancer associate with a decreased risk of metastasis[61], and a negative correlation between macrophage abundance and survival in patients with follicular lymphoma was potentially reversed with rituximab[62,63]. Critical for immunotherapies is a deeper understanding of the biophysics of the tumour microenvironment, including how various IgGs diffuse and function and how immune cells infiltrate and interact. In particular, subsaturating doses of opsonizing anti-Tyrp1 are highly effective against CD47-disrupted targets, with deep disruption of CD47 or SIRPα necessary for efficacy (Fig. 1f). SIRPα-KO CIM progenitors indeed showed better efficacy than anti-SIRPα engineered macrophages (Fig. 4d). Anti-SIRPα will dissociate, but inhibition via anti-SIRPα crosslinking (Extended Data Fig. 6d) is also a surprising biophysical mechanism that suggests a new class of checkpoint antagonists based on receptor crosslinkers. Nonetheless, limits to passive permeation of opsonizing and blocking antibodies can potentially be overcome with engineered macrophages (as we show in this work and as has been shown elsewhere[64,65]) because they can actively permeate through tight spaces[11] and potentially contribute to acquired immunity with phagocytic feedback. Lastly, chemotherapy had been observed long ago in cancer patient samples to cause mononuclear macrophages in cooperation with giant fused macrophages to engulf keratinized tumour cells[66], and so future studies should address possible connections to phase separation in tumours of highly phagocytic macrophages even in the absence of a chemotherapy.

Methods

Cell culture

All cell cultures were maintained in a humidified incubator at 37 °C, 5% CO_2. Basal media were supplemented with 10% (v/v) FBS (Sigma F2442), 100 U ml^{-1} penicillin and 100 µg ml^{-1} streptomycin (1% P/S, Gibco 15140122). B16-F10 (CRL-6475) cells were obtained from American Type Culture Collection (ATCC) and cultured in either RPMI-1640 (Gibco 11835-030) or Dulbecco's modified Eagle medium (DMEM; Corning 10-013-CV or Gibco 11995-065). B16 KO cell lines were generated as described previously[67] using single guide RNA (sgRNA) constructs targeting *Cd47* (5′-TCCCCGTAGAGATTACAATG) and *Tyrp1* (5′- CTTGTGGCAATGACAAATTG) and cultured under the same conditions as the parental WT B16-F10 cell line. J774A.1 mouse macrophages (ATCC TIB-67) and TC-1 cells (generously provided by Dr Sunil Singhal from the University of Pennsylvania) were both cultured in RPMI-1640. YUMM2.1 cells expressing GFP (a gift from Dr Chi Van Dang at the Wistar Institute) and CT-2A EGFRvIII cells (described previously[54]) were cultured in DMEM. RM-9 (ATCC CRL-3312) were cultured in DMEM:F12 (Gibco 11320-033).

Antibodies

Antibodies used for in vivo treatment and blocking, in vitro phagocytosis, western blotting, immunofluorescence microscopy and flow cytometry are reported in Supplementary Tables 1–3.

Mice

C57BL/6J mice (Jackson Laboratory 000664) were 6–12 weeks old at the time of first challenge unless otherwise specified. Age-matched mice were used as controls in re-challenge experiments. NSG mice aged 6–12 weeks old were obtained from the Stem Cell & Xenograft Core at the University of Pennsylvania. All experiments were performed in accordance with protocols approved by the Institutional Animal Care and Use Committee of the University of Pennsylvania.

BMDMs

Bone marrow was collected from donor mice, lysed with ACK buffer (Gibco A1049201) to deplete RBCs and cultured on Petri dishes for 7 days in Iscove's modified Dulbecco's medium (Gibco 12440053) supplemented with 10% FBS, 1% P/S and 20 ng ml^{-1} recombinant mouse macrophage colony-stimulating factor (M-CSF, BioLegend 576406). Successful differentiation was confirmed by flow cytometry staining with antibodies against macrophage markers. Cytokine-primed BMDMs were cultured in RPMI growth medium + 20 ng ml^{-1} M-CSF + 20 ng ml^{-1} IFNγ (BioLegend 575302) or 20 ng ml^{-1} IL-4 (BioLegend 574302) for 48 h before use in tumouroid assays or before analysis of protein expression by flow cytometry. For immunofluorescence microscopy, differentiated BMDMs were detached and re-plated on bare glass coverslips at a density of ~5.5×10^3 per cm^2 in RPMI growth medium + 20 ng ml^{-1} M-CSF. Cytokines were added 3 h later when cells were mostly attached to the glass, and cells were fixed and stained 48 h later.

CIM progenitors and gene KO

CIM progenitors were generated previously[45,46]. For KO of SIRPα by CRISPR–Cas9, CIMs were transduced with a lentiviral expression system. The sgRNA targeting *Sirpa* (5′-TAATTCTAAGGTCATCTGCG) was designed with the Broad sgRNA design algorithm and cloned into the lenti-sgRNA blast vector (Addgene plasmid 104993) using a BsmBI restriction digest. Plasmids pMD2.G and psPAX2 were used to generate lentivirus with HEK293T cells as previously described[46]. CIMs were cultured in suspension in 10 cm Petri dishes in RPMI-1640 (Gibco A1049101) supplemented with 10% FBS and 1% P/S. Medium was also supplemented with 2 μM β-oestrogen (Sigma-Aldrich E2758-250MG) and 10 ng ml^{-1} recombinant mouse GM-CSF (BioLegend 576302). Cells were passaged every 2 days at subconfluent concentration of 1×10^5 cells ml^{-1}. To differentiate for phagocytosis assays, cells were washed twice with 5% FBS/PBS to remove excess β-oestrogen and plated in DMEM supplemented with 10% FBS, 1% P/S and 20 ng ml^{-1} recombinant mouse M-CSF for 7 days.

In vitro phagocytosis

For 2D phagocytosis assays, BMDMs were detached and re-plated in 24-well plates at a density of 1.8×10^4 per cm^2 in Iscove's modified Dulbecco's medium supplemented with 10% FBS, 1% P/S and 20 ng ml^{-1} M-CSF. The next day, BMDMs were labelled with 0.5 μM CellTracker Deep Red dye (Invitrogen C34565) according to the manufacturer's protocol. Following staining, macrophages were washed and incubated in serum-free medium supplemented with 0.1% (w/v) bovine serum albumin (BSA). In some experiments, target cells were labelled with carboxyfluorescein diacetate succinimidyl ester (Invitrogen V12883) also according the manufacturer's protocol. B16 were detached and opsonized in serum-free medium for 30 min on ice with 10–20 μg ml^{-1} anti-Tyrp1, with mouse IgG2a isotype control antibody, or with 5% (v/v) mouse serum collected during the course of tumour challenge as described below. RM-9, TC-1 and CT-2A were opsonized similarly with 10 μg ml^{-1} anti-GD2, 25 μg ml^{-1} anti-mRBC and 5% (v/v) serum, respectively. For CD47 blockade experiments, 20 μg ml^{-1} anti-CD47 or rat IgG2a isotype control antibody was added during opsonization. For SIRPα blockade, 10 μg ml^{-1} anti-SIRPα was added to adherent BMDMs at 37 °C at this time. Opsonized B16 suspensions were added to BMDMs at a ~2:1 ratio and incubated at 37 °C, 5% CO_2 for 2 h. Non-adherent cells were removed by washing with PBS, and the remaining cells were fixed with 4% formaldehyde, counterstained with Hoechst 33342 (Invitrogen H3570), and imaged on an Olympus IX71 inverted microscope with a 40×/0.6 numerical aperture (NA) or 20×/0.4 NA objective. The Olympus IX71 microscope was equipped with a Prime sCMOS camera (Photometrics) and a pE-300 LED illuminator (CoolLED), which were controlled with μManager software v1.4 or v2 (ref. 68).

To visualize SIRPα on phagocytic macrophages, assays were performed similarly using J774A.1 mouse macrophages to which mouse RBCs opsonized with anti-mouse RBC were added. Staining for SIRPα and phospho-tyrosine was performed as previously described[44].

Tumouroids

To generate surfaces conducive to B16 tumouroid formation, 96-well plates (Greiner Bio-One 650161) were either coated with 70 μl of 2% agarose in water or PBS or, more commonly, treated for 20 min with 100 μl anti-adherence rinsing solution (StemCell Technologies 07010). The wells were washed with PBS, and then blocked with 0.5–1% (w/v) BSA (Sigma) at 37 °C for 1 h. B16 were detached by brief trypsinization, resuspended in RPMI supplemented with 10% FBS, 1× non-essential amino acid solution (Gibco 11140050) and 1 mM sodium pyruvate (Gibco 11360070) at a concentration of 1×10^3 or 1×10^4 per millilitre, and added to passivated wells in a volume of 100 μl. A single aggregate of B16 cells formed in each well, typically within 12 h. For tumouroid disaggregation studies, EDTA or EGTA was added in PBS to obtain a final concentration of 2 mM, and in some cases magnesium sulfate was also added for a final concentration of 5 mM Mg^{2+}. Similarly, Latrunculin A (Invitrogen L12370) dissolved at 1 mM in dimethyl sulfoxide (DMSO) was further diluted in PBS and added to obtain a final concentration of 1 μM. For phagocytosis versus growth studies, CellTracker Deep Red-labelled BMDMs and antibodies (final concentration 20 μg ml^{-1} anti-Tyrp1 and/or 20 μg ml^{-1} anti-CD47 or 10 μg ml^{-1} anti-SIRPα unless otherwise specified) or mouse serum (final concentration 1:200) were added 24 h later in a volume of 20 μl RPMI growth medium with 120 ng ml^{-1} M-CSF. For myosin-II inhibition studies, 20 μM *p*-amino-blebbistatin (Cayman Chemical 22699-500) or an equal volume of DMSO vehicle was added to B16 tumouroids for 1 h before addition of BMDMs. The *p*-amino form of blebbistatin was used for enhanced photostability and solubility and to limit phototoxicity and interference measuring GFP fluorescence. Tumouroids were imaged on the Olympus IX71 microscope with 20×/0.4 NA, 10×/0.3 NA or 4×/0.13 NA objectives. Tumouroid projected areas were measured in Fiji/ImageJ (ref. 69) after thresholding GFP fluorescence using built-in thresholding algorithms (MaxEntropy or Li) and manually adjusting the threshold as needed.

Macrophage aggregate monocultures were prepared similarly in anti-adherence rinsing solution-treated 96-well plates by adding 100 μl suspensions containing 1×10^3 BMDMs with 20 ng ml^{-1} M-CSF in RPMI growth medium to each well. For cytokine studies, IFNγ or IL-4 was added the next day in a volume of 20 μl RPMI growth medium for a final concentration of 20 ng ml^{-1}. For myosin-II inhibition studies, blebbistatin (EMD Millipore 203390) or *p*-amino-blebbistatin was added in a volume of 20 μl RPMI growth medium for a final drug concentration of 20 μM.

For confocal imaging, tumouroids were fixed ~20 h after addition of BMDMs and antibodies by adding an equal volume of 4% (w/v) formaldehyde directly to the media in each well for 30 min at room temperature. Half of this solution was removed and replaced with an equal volume of 2% (w/v) formaldehyde for 30 min. The tumouroids were washed with PBS to remove fixative, repeating the procedure of removing and replacing half the volume at each step. The fixed tumouroids were transferred via a wide-bore pipette tip to an eight-well chambered coverglass (Lab-Tek) and counterstained with 5 μg ml^{-1} Hoechst 33342. Confocal images were acquired on a Leica TCS SP8 with a 20×/0.75 NA objective. Radial fluorescence profiles were calculated in ImageJ by thresholding maximum intensity projections of GFP and

Deep Red fluorescence and calculating the tumouroid centroid, which was used as the input for $r = 0$ in the Radial Profile ImageJ plugin applied individually to the GFP and Deep Red channels. This plugin calculates the average fluorescence intensity $I(r)$ for a circle of radius r centred at the inputted position of the tumouroid centroid. $I(r)$ values were normalized by dividing by the total average fluorescence intensity $\Sigma I(r)$ for all r.

Entropy image analysis

Fluorescence images of CellTracker Deep-Red-labelled macrophages were converted to binary images of black cells on a white background using the Otsu threshold algorithm in ImageJ. The number of dark pixels was determined from the image histogram, and the image was saved as a PNG file, which is a form of lossless file compression, to determine the compressed file size as a measure of entropy. Random images for normalization and structured images were generated using the Python NumPy and PIL/Pillow packages and analysed with Fiji/ImageJ. Python code is provided in Supplementary Information.

Transcriptomic analysis

Public microarray data for BMDMs treated with IFNγ for 18 h versus control BMDMs (GSE60290) (ref. 70) and for BMDMs treated with IL-4 for 24 h versus control BMDMs (GSE69607) (ref. 71) were accessed through the National Center for Biotechnology Information Gene Expression Omnibus (GEO) repository and analysed using the GEO2R interactive web tool (https://www.ncbi.nlm.nih.gov/geo/geo2r/). Differential expression was considered significant for $P < 0.05$, where the adjusted P values were computed by the default method in GEO2R that uses the false discovery rate method of Benjamini and Hochberg. The B16-F10 RNA-seq dataset (GSE162105) (ref. 72) analysed for cell adhesion genes was also accessed through the GEO repository.

Flow cytometry

Phagocytosis of B16 by macrophages in tumouroids was assessed by pooling identically treated tumouroids from a single 96-well plate, disaggregating them to single-cell suspensions and analysing cell suspensions by flow cytometry. Tumouroids were collected into fluorescence-activated cell sorting (FACS) buffer (PBS plus 1% (w/v) BSA and 0.1% (w/v) sodium azide) ~18 h after addition of BMDMs ± anti-Tyrp1, pelleted by centrifugation and resuspended in FACS buffer + 0.5 mM EDTA for 15–30 min at room temperature. The suspension was pipetted up and down until the cells were deemed to be disaggregated by inspection on a haematocytometer. Viable cells were distinguished by staining with Zombie aqua fixable viability dye (BioLegend 423101) in PBS for 15 min at room temperature. The cells were washed with FACS buffer, fixed with 4% (w/v) formaldehyde for 15 min at room temperature and stored at 4 °C until analysis. Flow cytometry was performed on a BD LSRII (Benton Dickinson), and data were analysed with FCS Express 7 software (De Novo Software). Doublets, cell debris and non-viable cells were excluded, and GFP^+ $DeepRed^+$ events were considered phagocytic macrophages.

For mAb and serum binding analyses to tumour cell lines, B16, YUMM2.1, RM-9 or CT-2A cells were detached, washed and resuspended in FACS buffer containing primary antibody or 5% (v/v) mouse serum collected as described below. Cell suspensions were incubated at 4 °C for 30 min and agitated to prevent cell settling. Cells were washed three times with FACS buffer and incubated with fluorophore-conjugated secondary antibodies in FACS buffer for 30 min at 4 °C and later with PE–streptavidin if required to label biotinylated anti-mouse IgG3. Finally, cells were washed three times and resuspended in FACS buffer containing 0.2 μg ml^{-1} 4′,6-diamidino-2-phenylindole (Cell Signaling Technology). For samples that could not be analysed on the day of staining and required fixation, cells were stained with Zombie aqua fixable viability dye in PBS for 15 min at room temperature before staining with antibodies or serum, and 4′,6-diamidino-2-phenylindole was omitted from the final fixed cell suspension. Those samples were fixed with FluoroFix Buffer (BioLegend 422101) or 2–4% (w/v) formaldehyde. For experiments analysed in the same plot, the same lots of primary and secondary antibodies and identical staining conditions were used. When these analyses were performed on different days, UltraRainbow calibration beads (Spherotech URCP-38-2K) were used to adjust the photomultiplier tube voltage in each channel to maintain the median fluorescence intensity of the brightest peak within a tolerance of ±5%.

For surface marker expression on BMDMs and CIMs, samples were prepared and analysed similarly to cell lines except that Fc receptors were blocked with 10 μg ml^{-1} anti-mouse CD16/CD32 clone 2.4G2 (BD Biosciences 553142) and 2.5 μg ml^{-1} anti-mouse CD16.2 clone 9E9 (BioLegend 149502) for 10 min on ice before addition of fluorophore-conjugated antibodies. Blocking antibodies were excluded from samples of BMDMs stained for Fc receptors.

Tumour models

B16, RM-9 and TC-1 cell lines were detached by brief trypsinization, washed with PBS and resuspended at 2×10^6 per millilitre in PBS. Cell suspensions remained on ice until injection. Fur on the injection site (usually the right flank) was wet slightly with a drop of 70% ethanol and brushed aside to visualize the skin. A 100 μl bolus (containing 2×10^5 tumour cells) was injected beneath the skin in the subcutaneous model or intravenously in the experimentally induced lung metastasis model. Treated mice with B16 tumours received i.v. injections of anti-Tyrp1 (250 μg antibody in 100 μl PBS) via the lateral tail vein on days 4, 5, 7, 11, 13 and 15 post tumour cell inoculation. Where indicated, mice also received i.v. injections of anti-CD47 (83 μg antibody dosed in the same in 100 μl PBS volume as anti-Tyrp1). Mice with RM-9 tumours received 250 μg (in 100 μl PBS) anti-GD2 intravenously on the same schedule instead of anti-Tyrp1. Tumours were monitored by palpation and measured with digital callipers. The projected area was roughly elliptical and calculated as $A = \pi/4 \times L \times W$ where L is the length along the longest axis and W is the width measured along the perpendicular axis. A projected area of 125 mm^2 was considered the terminal tumour burden for survival analyses.

For B16 pre-opsonization, tumour cells were prepared as above with resuspension at 1×10^7 cells ml^{-1} in PBS containing 10 μg ml^{-1} anti-Tyrp1, 10 μg ml^{-1} mIgG2a isotype control or 5% (v/v) convalescent serum and incubated for 30 min on ice. For TC-1 pre-opsonization experiments, tumour cells were incubated with 25 μg ml^{-1} anti-mRBC and 10 μg ml^{-1} anti-CD47 in the same manner. Just before subcutaneous injection, pre-opsonized cell suspensions were diluted 1:5 to the target density of 2×10^6 cells ml^{-1} in PBS.

Serum collection

Blood was drawn retro-orbitally and allowed to clot for 30–60 min at room temperature in a microcentrifuge tube. The serum was separated from the clot by centrifugation at 1,500*g* and stored at −20 °C for use in flow cytometry, phagocytosis assays and western blotting.

Immune infiltrate analysis of tumours

For flow cytometry of immune cell markers in tumours, mice were treated with a single dose of i.v. anti-Tyrp1 at day 4 (96 h) post inoculation and killed 24 h later. Tumours were photographed, then excised and placed into 5% FBS/PBS. Tumours were then disaggregated with Dispase (Corning 354235) supplemented with 3 mg ml^{-1} Collagenase Type IV (Gibco 17104019) and DNaseI (Sigma-Aldrich 10104159001) for 30 min at 37 °C, centrifuged for 5 min at 300*g* and resuspended in 1 ml of ACK lysing buffer for 12 min at room temperature. Samples were centrifuged for 5 min at 300*g*, washed with FACS buffer and incubated in FACS buffer containing fluorophore-conjugated antibodies to immune markers on ice for 30 min. Samples were then washed with FACS buffer and fixed with FluoroFix Buffer for 30 min at room temperature before analysis on a flow cytometer.

For immunofluorescence staining of tumour sections, mice were treated in the same manner. Whole tumours were then excised, fixed in 4% paraformaldehyde overnight at 4 °C and stored in 70% ethanol. The Comparative Pathology Core (University of Pennsylvania) embedded the tissues in paraffin, and sectioned and stained the tumour sections with anti-F4/80 according to their standardized protocols. Sections were imaged on the Olympus IX71 microscope as described above. Radial profile analysis was conducted with the Radial Profile Plot plugin for ImageJ. Sectioning and trichrome staining of B16 tumours were performed by the Molecular Pathology and Imaging Core (University of Pennsylvania). Tile scan images of the trichrome-stained tumour section were acquired on the EVOS FL Auto Imager with a 10×/0.25 NA objective (Thermo Fisher).

Adoptive cell transfers

Fresh bone marrow was collected as above through the RBC lysis step. Marrow cells were then counted on a haemocytometer and resuspended at 8×10^7 cells ml^{-1} in 5% FBS/PBS. To block SIRPα, cells were incubated with anti-SIRPα (18 μg ml^{-1}) for 45 min at room temperature on a rotator, centrifuged to remove unbound P84 and resuspended again at 8×10^7 cells ml^{-1} in 2% FBS/PBS with or without 1 mg ml^{-1} anti-Tyrp1. Marrow cells (2×10^7 cells in 250 μl 2% FBS/PBS) were injected intravenously into tumour-bearing mice 4 days after tumour engraftment. SIRPα KO CIM progenitors (4×10^6 cells in 250 μl 2% FBS/PBS with 1 mg ml^{-1} anti-Tyrp1 or anti-GD2) were injected intravenously in the same manner.

Immunofluorescence staining and microscopy

B16 and RM-9 cells were cultured for 24 h on glass-bottom dishes (MatTek) coated with 10 μg ml^{-1} fibronectin from human plasma (Corning 354008) to facilitate attachment. The cells were fixed with 4% paraformaldehyde, blocked in 1% (w/v) BSA or 5% (v/v) normal donkey serum in PBS, and stained with primary (anti-Tyrp1 or anti-GD2) and secondary antibodies diluted in blocking buffer with 5 μg ml^{-1} Hoechst 33342 counterstain. The cells were imaged on the Olympus IX71 with a 60×/1.2 NA oil objective. BMDMs were cultured on bare in the presence of cytokines coverslips as described above for 48 h and then fixed with 4% paraformaldehyde for 15 min at room temperature and permeabilized with 0.2% v/v Triton X-100 for 10 min at room temperature. The fixed, permeabilized cells were blocked in 5% (v/v) normal donkey serum in PBS, stained with primary (anti-lamin A/C and anti-lamin B1) and secondary antibodies, and counterstained with 1 μg ml^{-1} Hoechst 33342. Stained coverslips were mounted on glass slides with ProLong Gold Antifade (Thermo Fisher Scientific P36930) and imaged on the Olympus IX71 with a 40×/0.6 NA objective.

Western blotting

Lysate was prepared from B16 CD47 KO cells using RIPA buffer containing 1× protease inhibitor cocktail (Sigma P8340) and boiled in 1× NuPage LDS sample buffer (Invitrogen NP0007) with 2.5% (v/v) β-mercaptoethanol. For detection of N-cadherin, B16 proteins were fractionated by ultracentrifugation. Proteins were separated by electrophoresis in NuPAGE 4–12% Bis-Tris gels run with 1× MOPS buffer (Invitrogen NP0323) and transferred to an iBlot nitrocellulose membrane (Invitrogen IB301002). The membranes were blocked with 5% non-fat milk in Tris-buffered saline (TBS) plus 0.1% (w/v) Tween-20 (TBST) for 1 h and stained with primary antibodies or with 5% (v/v) mouse serum overnight at 4 °C with agitation. The membranes were washed with TBST and incubated with 1:500 secondary antibody conjugated with horseradish peroxidase or with 1:5,000 secondary antibody conjugated with IRDye800CW in 5% milk in TBST for 1 h at room temperature with agitation. The membranes were washed again three times with TBST, then TBS. Membranes probed with horseradish-peroxidase-conjugated secondary were developed with a 3,3′,5,5′-teramethylbenzidine substrate (Genscript L0022V or Sigma T0565). Developed membranes were scanned and analysed with ImageJ. Membranes probed with IRDye800CW-conjugated secondary were imaged on an Odyssey near-infra-red scanner (LiCor). Uncropped blots and details of cropping are shown in Supplementary Figs. 3 and 5.

Pipette aspiration rheology

Tumouroids were formed in non-adhesive well plates and transferred via wide-bore pipette to a glass-bottom dish. Fresh tumours were collected and stored in RPMI + 10% FBS. The tumour was held in a chamber consisting of glass coverslips separated by silicone spacers on three sides and filled with RPMI + 10% FBS. For aspiration of the tumour interior or for large tumours, the tumour was sliced with a scalpel or razor blade before placement in the chamber. A glass capillary (1 mm outer diameter/0.75 mm inner diameter, World Precision Instruments TW100-3) was pulled on a Browning/Flaming type pipette puller (Sutter Instruments P-97), scored with a ceramic tile and broken to obtain micropipettes with diameters 40–100 μm. Only cleanly broken tips were used for aspiration. When required, micropipettes were bent with a De Fonbrune microforge. The micropipette was backfilled with 3% (w/v) BSA in PBS to prevent tissue adhesion and connected to a dual-stage water manometer. Aspiration was applied manually with a syringe (0.5–10 ml), and the pressure difference ΔP was measured with a calibrated pressure transducer (Validyne). Time-lapse brightfield microscopy of aspiration was performed on a TE300 inverted microscope (Nikon) with a 20×/0.5 NA objective and images were acquired on an Evolve Delta EMCCD camera (Photometrics) using μManager v1.4 or v2 software. Tissue elongation $L(t)$ was determined by image analysis with Fiji/ImageJ and fit to the standard linear solid model[73] assuming a wall shape parameter Φ of ~2. Tumour strain typically reached a plateau value after several seconds that was maintained for the short timescale of these experiments, allowing the elastic modulus to be approximated as $E \sim \Delta P (L/R_P)^{-1}$ as described previously, where R_P is the pipette radius[30]. Tumouroid flow on longer timescales was modelled by including a viscosity term in the standard linear model[32].

Fluorescence recovery after photobleaching

Confocal time-lapse imaging was performed at 37 °C with 5% CO_2 in a humidified chamber with an SP8 inverted laser scanning confocal microscope. Time-lapse images were acquired with a 63×/1.4 NA oil immersion objective up to 10 min after photobleaching. Cells were imaged in phenol-red-free low-glucose DMEM (Gibco 11054-020) with 10% FBS and 1% P/S. Image sequences were analysed using Fiji/ImageJ.

Statistical analysis and curve fitting

Statistical analyses and curve fitting were performed in Prism v8.4-v9.5 (GraphPad). Hypothesis testing was used to assess the null hypothesis that the means of groups being compared are the same. Details for each analysis are provided in figure captions, and exact P values are provided. Standard assumptions were made regarding the normality of the data, the homogeneity of the variances among groups (except for Welch's t-test) and the independence of measurements. Tumouroid and tumour growth data (projected area versus time) were fit to the exponential growth model ($A(t) = A_0 e^{kt}$ for tumours and $A(t) = A_1 e^{k(t-1)}$ for tumouroids) using non-linear least squares regression with pre-factors A_0 or A_1, and exponential growth rate k. In some experiments, early tumour growth was fit to a linear model $A(t) = A_0 + kt$. In tumouroid experiments, outliers in samples of the fitted parameter k were identified by ROUT's method (maximum false discovery rate, $Q = 1\%$) in Prism. Cleaned data were fit to mathematical models described in Supplementary Fig. 3 for the dependence of k on macrophage number. Akaike's information criterion was used to compare which one of two models better fit the data under the null hypothesis that the simpler model with fewer parameters was correct. The extra sum-of-squares F-test was used to assess fitted parameters for data from two different experimental conditions under the null hypothesis that the parameters were shared for both datasets.

Reporting summary

Further information on research design is available in the Nature Portfolio Reporting Summary linked to this article.

Data availability

The main data supporting the results in the study are available within the paper and its Supplementary Information. Source data are provided with this paper. Source data for the tumour-growth curves in Figs. 3f and 6c and in Extended Data Figs. 6a and 9a,b are provided with this paper. No large sequencing datasets were generated as part of this study, yet publicly available data from The Cancer Genome Atlas, The Human Protein Atlas and the National Center for Biotechnology Information GEO repository were accessed via the identifiers provided in Methods and in the relevant figure captions.

Code availability

Python code to generate random and structured simulated images is provided in Supplementary Information.

References

1. Chen, J. et al. SLAMF7 is critical for phagocytosis of haematopoietic tumour cells via Mac-1 integrin. *Nature* **544**, 493 (2017).
2. Morioka, S. et al. Efferocytosis induces a novel SLC program to promote glucose uptake and lactate release. *Nature* **563**, 714–718 (2018).
3. Vorselen, D. et al. Microparticle traction force microscopy reveals subcellular force exertion patterns in immune cell–target interactions. *Nat. Commun.* **11**, 20 (2020).
4. Nia, H. T., Munn, L. L. & Jain, R. K. Physical traits of cancer. *Science* **370**, eaaz0868 (2020).
5. Manning, M. L., Foty, R. A., Steinberg, M. S. & Schoetz, E. M. Coaction of intercellular adhesion and cortical tension specifies tissue surface tension. *Proc. Natl Acad. Sci. USA* **107**, 12517–12522 (2010).
6. Ohno, S. et al. The degree of macrophage infiltration into the cancer cell nest is a significant predictor of survival in gastric cancer patients. *Anticancer Res.* **23**, 5015–5022 (2003).
7. Ohno, S. et al. Correlation of histological localization of tumor-associated macrophages with clinicopathological features in endometrial cancer. *Anticancer Res.* **24**, 3335–3342 (2004).
8. Zindel, J. et al. Primordial GATA6 macrophages function as extravascular platelets in sterile injury. *Science* **371**, 0–13 (2021).
9. Flores-Toro, J. A. et al. CCR2 inhibition reduces tumor myeloid cells and unmasks a checkpoint inhibitor effect to slow progression of resistant murine gliomas. *Proc. Natl Acad. Sci. USA* **117**, 1129–1138 (2020).
10. Georgouli, M. et al. Regional activation of myosin II in cancer cells drives tumor progression via a secretory cross-talk with the immune microenvironment. *Cell* **176**, 757–774.e23 (2019).
11. Alvey, C. M. et al. SIRPA-inhibited, marrow-derived macrophages engorge, accumulate, and differentiate in antibody-targeted regression of solid tumors. *Curr. Biol.* **27**, 2065–2077.e6 (2017).
12. Willingham, S. B. et al. The CD47-signal regulatory protein alpha (SIRPa) interaction is a therapeutic target for human solid tumors. *Proc. Natl Acad. Sci. USA* **109**, 6662–6667 (2012).
13. Morrissey, M. A., Kern, N. & Vale, R. D. CD47 ligation repositions the inhibitory receptor SIRPA to suppress integrin activation and phagocytosis. *Immunity* **53**, 290–302.e6 (2020).
14. Bakalar, M. H. et al. Size-dependent segregation controls macrophage phagocytosis of antibody-opsonized targets. *Cell* **174**, 131–142.e13 (2018).
15. Advani, R. et al. CD47 blockade by Hu5F9-G4 and rituximab in non-Hodgkin's lymphoma. *N. Engl. J. Med.* **379**, 1711–1721 (2018).
16. Jalil, A. R., Andrechak, J. C. & Discher, D. E. Macrophage checkpoint blockade: results from initial clinical trials, binding analyses, and CD47-SIRPα structure–function. *Antib. Ther.* **3**, 80–94 (2020).
17. Lakhani, N. J. et al. Evorpacept alone and in combination with pembrolizumab or trastuzumab in patients with advanced solid tumours (ASPEN-01): a first-in-human, open-label, multicentre, phase 1 dose-escalation and dose-expansion study. *Lancet Oncol.* **22**, 1740–1751 (2021).
18. Kamber, R. A. et al. Inter-cellular CRISPR screens reveal regulators of cancer cell phagocytosis. *Nature* **597**, 549–554 (2021).
19. Chao, M. P. et al. Calreticulin is the dominant pro-phagocytic signal on multiple human cancers and is counterbalanced by CD47. *Sci. Transl. Med.* **2**, 63ra94 (2010).
20. Ingram, J. R. et al. Localized CD47 blockade enhances immunotherapy for murine melanoma. *Proc. Natl Acad. Sci. USA* **114**, 10184–10189 (2017).
21. Tsai, R. K., Rodriguez, P. L. & Discher, D. E. Self inhibition of phagocytosis: the affinity of 'marker of self' CD47 for SIRPα dictates potency of inhibition but only at low expression levels. *Blood Cells. Mol. Dis.* **45**, 67–74 (2010).
22. Suter, E. C. et al. Antibody:CD47 ratio regulates macrophage phagocytosis through competitive receptor phosphorylation. *Cell Rep.* **36**, 109587 (2021).
23. Moynihan, K. D. et al. Eradication of large established tumors in mice by combination immunotherapy that engages innate and adaptive immune responses. *Nat. Med.* **22**, 1402–1410 (2016).
24. Zhu, E. F. et al. Synergistic innate and adaptive immune response to combination immunotherapy with anti-tumor antigen antibodies and extended serum half-life IL-2. *Cancer Cell* **27**, 489–501 (2015).
25. Sockolosky, J. T. et al. Durable antitumor responses to CD47 blockade require adaptive immune stimulation. *Proc. Natl Acad. Sci. USA* **113**, E2646–E2654 (2016).
26. Wang, S., He, Z., Wang, X., Li, H. & Liu, X. S. Antigen presentation and tumor immunogenicity in cancer immunotherapy response prediction. *eLife* **8**, e49020 (2019).
27. Liu, X. et al. CD47 blockade triggers T cell–mediated destruction of immunogenic tumors. *Nat. Med.* **21**, 1209–1215 (2015).
28. Xu, M. M. et al. Dendritic cells but not macrophages sense tumor mitochondrial DNA for cross-priming through signal regulatory protein α signaling. *Immunity* **47**, 363–373.e5 (2017).
29. Higgins, H. W., Lee, K. C., Galan, A. & Leffell, D. J. Melanoma in situ: part II. Histopathology, treatment, and clinical management. *J. Am. Acad. Dermatol.* **73**, 193–203 (2015).
30. Majkut, S. et al. Heart-specific stiffening in early embryos parallels matrix and myosin expression to optimize beating. *Curr. Biol.* **23**, 2434–2439 (2013).
31. Foty, R. A. & Steinberg, M. S. The differential adhesion hypothesis: a direct evaluation. *Dev. Biol.* **278**, 255–263 (2005).
32. Guevorkian, K., Colbert, M. J., Durth, M., Dufour, S. & Brochard-Wyart, F. Aspiration of biological viscoelastic drops. *Phys. Rev. Lett.* **104**, 218101 (2010).
33. Khalil, D. N. et al. An open-label, dose-escalation phase I study of anti-TYRP1 monoclonal antibody IMC-20D7S for patients with relapsed or refractory melanoma. *Clin. Cancer Res.* **22**, 5204–5211 (2016).
34. Matlung, H. L. et al. Neutrophils kill antibody-opsonized cancer cells by trogoptosis. *Cell Rep.* **23**, 3946–3959.e6 (2018).
35. Velmurugan, R., Challa, D. K., Ram, S., Ober, R. J. & Ward, E. S. Macrophage-mediated trogocytosis leads to death of antibody-opsonized tumor cells. *Mol. Cancer Ther.* **15**, 1879–1889 (2016).
36. Martiniani, S., Chaikin, P. M. & Levine, D. Quantifying hidden order out of equilibrium. *Phys. Rev. X* **9**, 11031 (2019).

37. Kakuta, S., Tagawa, Y. I., Shibata, S., Nanno, M. & Iwakura, Y. Inhibition of B16 melanoma experimental metastasis by interferon-γ through direct inhibition of cell proliferation and activation of antitumour host mechanisms. *Immunology* **105**, 92–100 (2002).
38. Ammon, C. et al. Comparative analysis of integrin expression on monocyte-derived macrophages and monocyte-derived dendritic cells. *Immunology* **100**, 364–369 (2000).
39. McNally, A. K. & Anderson, J. M. β1 and β2 integrins mediate ddhesion during macrophage fusion and multinucleated foreign body giant cell formation. *Am. J. Pathol.* **160**, 621–630 (2002).
40. Lehmann, B. et al. Tumor location determines tissue-specific recruitment of tumor-associated macrophages and antibody-dependent immunotherapy response. *Sci. Immunol.* **2**, eaah6413 (2017).
41. Okazawa, H. et al. Negative regulation of phagocytosis in macrophages by the CD47-SHPS-1 system. *J. Immunol.* **174**, 2004–2011 (2005).
42. Yanagita, T. et al. Anti-SIRPα antibodies as a potential new tool for cancer immunotherapy. *JCI Insight* **2**, e89140 (2017).
43. Motegi, S.-I. et al. Essential roles of SHPS-1 in induction of contact hypersensitivity of skin. *Immunol. Lett.* **121**, 52–60 (2008).
44. Tsai, R. K. & Discher, D. E. Inhibition of "self" engulfment through deactivation of myosin-II at the phagocytic synapse between human cells. *J. Cell Biol.* **180**, 989–1003 (2008).
45. Wang, G. G. et al. Quantitative production of macrophages or neutrophils ex vivo using conditional Hoxb8. *Nat. Methods* **3**, 287–293 (2006).
46. Roberts, A. W. et al. Cas9$^+$ conditionally-immortalized macrophages as a tool for bacterial pathogenesis and beyond. *eLife* **8**, e45957 (2019).
47. Trcka, J. et al. Redundant and alternative roles for activating Fc receptors and complement in an antibody-dependent model of autoimmune vitiligo. *Immunity* **16**, 861–868 (2002).
48. Meeth, K., Wang, J. X., Micevic, G., Damsky, W. & Bosenberg, M. W. The YUMM lines: a series of congenic mouse melanoma cell lines with defined genetic alterations. *Pigment Cell Melanoma Res.* **29**, 590–597 (2016).
49. Bruhns, P. Properties of mouse and human IgG receptors and their contribution to disease models. *Blood* **119**, 5640–5649 (2012).
50. Carmi, Y. et al. Allogeneic IgG combined with dendritic cell stimuli induce antitumour T-cell immunity. *Nature* **521**, 99–104 (2015).
51. Theruvath, J. et al. Anti-GD2 synergizes with CD47 blockade to mediate tumor eradication. *Nat. Med* **28**, 333–344 (2022).
52. Lin, K.-Y. et al. Treatment of established tumors with a novel vaccine that enhances Major Histocompatibility Class II presentation of tumor antigen. *Cancer Res.* **56**, 21–26 (1996).
53. Oldenborg, P.-A., Gresham, H. D. & Lindberg, F. P. Cd47-signal regulatory protein α (Sirpα) regulates Fcγ and complement receptor–mediated phagocytosis. *J. Exp. Med.* **193**, 855–862 (2001).
54. Ma, L. et al. Enhanced CAR–T cell activity against solid tumors by vaccine boosting through the chimeric receptor. *Science* **365**, 162–168 (2019).
55. Oldenborg, P.-A., Gresham, H. D., Chen, Y., Izui, S. & Lindberg, F. P. Lethal autoimmune hemolytic anemia in CD47-deficient nonobese diabetic (NOD) mice. *Blood* **99**, 3500–3504 (2002).
56. Mattes, M. J., Thomson, T. M., Old, L. J. & Lloyd, K. O. A pigmentation-associated, differentiation antigen of human melanoma defined by a precipitating antibody in human serum. *Int. J. Cancer* **32**, 717–721 (1983).
57. Fässler, M. et al. Antibodies as biomarker candidates for response and survival to checkpoint inhibitors in melanoma patients. *J. Immunother. Cancer* **7**, 50 (2019).
58. van Vloten, J. P. et al. Quantifying antigen-specific T cell responses when using antigen-agnostic immunotherapies. *Mol. Ther. Methods Clin. Dev.* **13**, 154–166 (2019).
59. Rodríguez, D. et al. Tumor microenvironment profoundly modifies functional status of macrophages: peritoneal and tumor-associated macrophages are two very different subpopulations. *Cell. Immunol.* **283**, 51–60 (2013).
60. Salmi, S. et al. The number and localization of CD68$^+$ and CD163$^+$ macrophages in different stages of cutaneous melanoma. *Melanoma Res.* **29**, 237–247 (2019).
61. Fiumara, A. et al. In situ evidence of neoplastic cell phagocytosis by macrophages in papillary thyroid cancer. *J. Clin. Endocrinol. Metab.* **82**, 1615–1620 (1997).
62. Taskinen, M., Karjalainen-Lindsberg, M. L. & Leppä, S. Prognostic influence of tumor-infiltrating mast cells in patients with follicular lymphoma treated with rituximab and CHOP. *Blood* **111**, 4664–4667 (2008).
63. Canioni, D. et al. High numbers of tumor-associated macrophages have an adverse prognostic value that can be circumvented by rituximab in patients with follicular lymphoma enrolled onto the GELA-GOELAMS FL-2000 trial. *J. Clin. Oncol.* **26**, 440–446 (2008).
64. Morrissey, M. A. et al. Chimeric antigen receptors that trigger phagocytosis. *eLife* **7**, e36688 (2018).
65. Sun, J. et al. Engineered proteins with sensing and activating modules for automated reprogramming of cellular functions. *Nat. Commun.* **8**, 477 (2017).
66. Burkhardt, A. & Gebbers, J.O. Giant cell stromal reaction in squamous cell carcinomata. *Virchows Arch. A Pathol. Anat. Histopathol* **375**, 263–280 (1977).
67. Hayes, B. H. et al. Macrophages show higher levels of engulfment after disruption of cis interactions between CD47 and the checkpoint receptor SIRPα. *J. Cell Sci.* **133**, jcs237800 (2020).
68. Edelstein, A., Amodaj, N., Hoover, K., Vale, R. & Stuurman, N. Computer control of microscopes using μManager. *Mol. Biol.* **92**, 14.20.1–14.20.17 (2010).
69. Schindelin, J. et al. Fiji: an open-source platform for biological-image analysis. *Nat. Methods* **9**, 676–682 (2012).
70. Hoeksema, M. A. et al. IFN-γ priming of macrophages represses a part of the inflammatory program and attenuates neutrophil recruitment. *J. Immunol.* **194**, 3909–3916 (2015).
71. Jablonski, K. A. et al. Novel markers to delineate murine M1 and M2 macrophages. *PLoS ONE* **10**, 5–11 (2015).
72. Dubrot, J. et al. In vivo screens using a selective CRISPR antigen removal lentiviral vector system reveal immune dependencies in renal cell carcinoma. *Immunity* **54**, 571–585.e6 (2021).
73. Sato, M., Theret, D. P., Wheeler, L. T., Ohshima, N. & Nerem, R. M. Application of the micropipette technique to the measurement of cultured porcine aortic endothelial cell viscoelastic properties. *J. Biomech. Eng.* **112**, 263–268 (1990).
74. Watanabe, T. et al. Higher cell stiffness indicating lower metastatic potential in B16 melanoma cell variants and in (−)-epigallocatechin gallate-treated cells. *J. Cancer Res. Clin. Oncol.* **138**, 859–866 (2012).
75. Liu, J. et al. Soft fibrin gels promote selection and growth of tumorigenic cells. *Nat. Mater.* **11**, 734–741 (2012).
76. Uhlén, M. et al. Tissue-based map of the human proteome. *Science* **347**, 1260419 (2015).
77. Yesmin, F. et al. Ganglioside GD2 enhances the malignant phenotypes of melanoma cells by cooperating with integrins. *Int. J. Mol. Sci.* **23**, 423 (2022).
78. Mosely, S. I. S. et al. Rational selection of syngeneic preclinical tumor models for immunotherapeutic drug discovery. *Cancer Immunol. Res.* **5**, 29–41 (2017).
79. Lechner, M. G. et al. Immunogenicity of murine solid tumor models as a defining feature of in vivo behavior and response to immunotherapy. *J. Immunother.* **36**, 477–489 (2013).

Acknowledgements
This work was supported by funding from the National Institutes of Health (NIH) and the National Science Foundation (NSF). D.E.D. discloses support for the research described in this study from NIH (U54 CA193417, U01 CA254886 and R01 HL124106), NSF (Materials Research Science and Engineering Center DMR-1720530 and DMR-1420530 and Grant Agreements CMMI 1548571 and 154857) and the Pennsylvania Department of Health (HRFF 4100083101). L.J.D. discloses support for the research described in this study from NIH (F32 CA228285). J.C.A and B.H.H. disclose support from the NSF (DGE-1845298). The content is solely the responsibility of the authors and does not necessarily represent the official views of the NIH or NSF. We thank C. Van Dang of the Wistar Institute for providing YUMM2.1 cells, S. Singhal for providing TC-1 cells and I. Brodsky of Penn Vet for providing editable CIM lines. We additionally thank J. Lee for aiding in development of the gene editing pipeline and S. Shin of Penn Vet for support on CIM progenitors. We acknowledge the following University of Pennsylvania core facilities: Cell Center, Stem Cell & Xenograft Core, Molecular Pathology & Imaging Core (supported by the Center for Molecular Studies in Digestive and Liver Diseases NIH/NIDDK Grant P30 DK050306), the Penn Vet Comparative Pathology Core, the Cell & Developmental Biology Microscopy Core, the Penn Cytomics & Cell Sorting Shared Research Laboratory (supported by the Abramson Cancer Center NIH/NCI Grant P30 CA016520) and the Penn Genomic Analysis Core.

Author contributions
J.C.A., L.J.D. and D.E.D. designed the research. J.C.A., L.J.D., B.H.H., S.K., W.Z., R.P. and J.I. performed experiments. J.C.A., L.J.D., B.H.H., S.K., W.Z., R.P., M.V. and J.I. analysed data. J.C.A., L.J.D., B.H.H., J.I. and C.M.A. developed methodology. L.M. provided materials. D.E.D. supervised the work. J.C.A., L.J.D. and D.E.D. wrote the paper.

Competing interests
The authors declare no competing interests.

Additional information
Extended data is available for this paper at https://doi.org/10.1038/s41551-023-01031-3.

Supplementary information The online version contains supplementary material available at https://doi.org/10.1038/s41551-023-01031-3.

Correspondence and requests for materials should be addressed to Dennis E. Discher.

Peer review information *Nature Biomedical Engineering* thanks George Georgiou, In-San Kim and the other, anonymous, reviewer(s) for their contribution to the peer review of this work. Peer reviewer reports are available.

https://doi.org/10.1038/s41551-023-01031-3

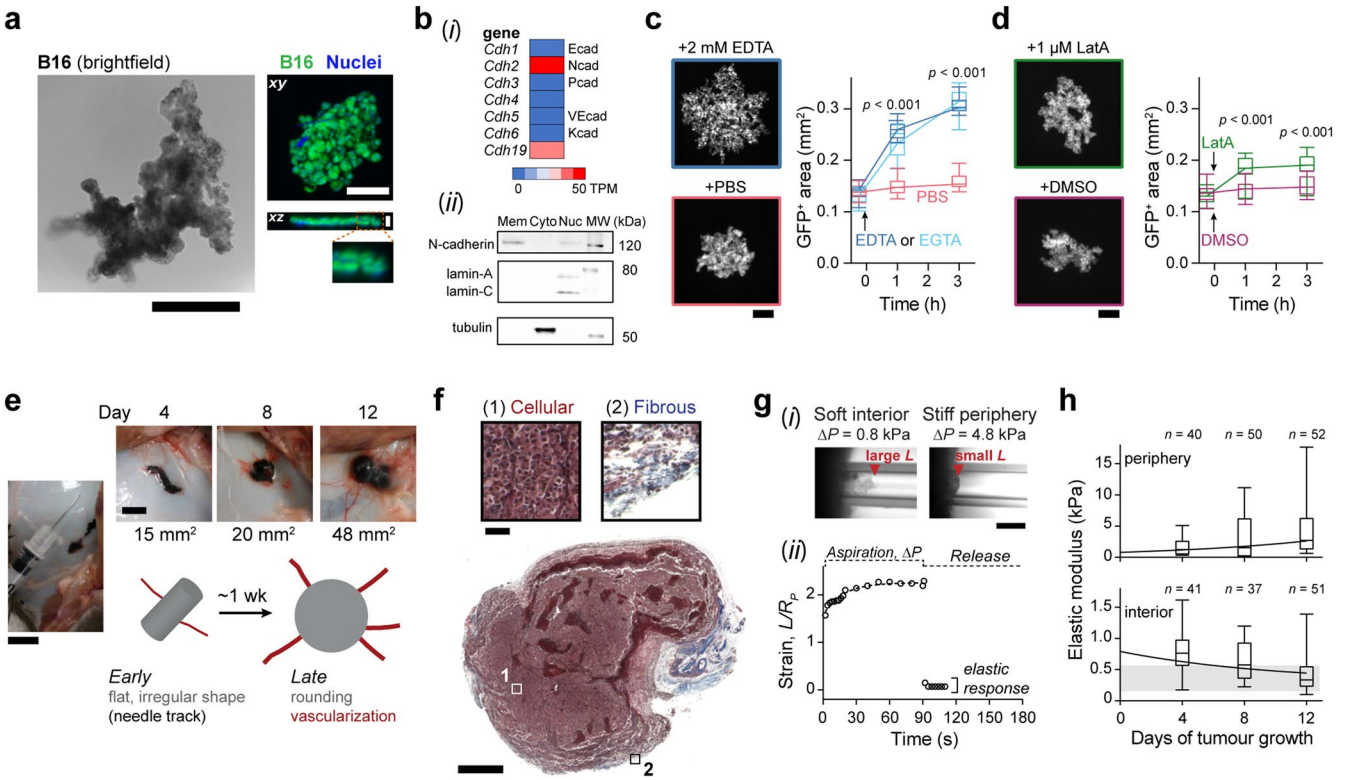

Extended Data Fig. 1 | Characterization of B16 tumouroids and subcutaneous tumours. a, Brightfield and confocal microscopy of B16 tumouroids. Left: Brightfield image of a B16 tumouroid three days after 1000 cells were seeded atop an agarose gel. Scale bar: 0.5 mm. Right: Confocal max intensity projections (*xy*, *xz* planes) of GFP (green) and Hoechst 33342 (blue) in a B16 tumouroid fixed ~24 h after 100 cells were seeded in a non-adhesive well. Scale bar: 100 μm. **b**-**d**, Tumouroid cohesion depends on Ca^{2+} and the actin cytoskeleton. Transcriptomic analysis (**b**-*i*) of cadherin gene expression in cultured B16 cells (GSE162105) (ref. 72) and immunoblotting (**b**-*ii*) of B16 membrane, cytoplasmic, and nuclear protein fractions for N-cadherin, lamin-A/C, and tubulin. The uncropped blots are shown in Supplementary Fig. 5. Tumouroid (GFP^+) area (**c**) following addition of 2 mM EDTA or EGTA ($n = 16$ tumouroids for PBS control or EGTA and $n = 14$ tumouroids for EDTA). In the box plots, the centreline is the median, the box is the interquartile range (IQR) from the 25th to 75th percentiles, and the whiskers extend over the entire range of the data. Statistical significance was assessed by one-way ANOVA at $t = 1$ h or 3 h, and adjusted p values were determined by Dunnett's multiple comparisons test between PBS and EDTA or EGTA ($p < 0.001$ for all comparisons). Representative images depict GFP fluorescence in tumouroids at $t = 3$ h after EDTA (top) and PBS (bottom) treatment. Scale bar: 200 μm. Tumouroid area (**d**) following addition of 1 μM Latrunculin A (LatA) or DMSO vehicle ($n = 16$ tumouroids per condition, box plot as described in **c**). Statistical significance was assessed by Welch's t-test (unpaired, two-tailed) between DMSO control and LatA treatment at $t = 1$ h or 3 h ($p < 0.001$ for both comparisons). Representative images depict GFP fluorescence in tumouroids at $t = 3$ h after treatment with LatA (top) and DMSO (bottom). Scale bar: 200 μm. **e**, Photographs of subcutaneous (s.c.) B16 tumours in mice dissected on day 4, 8, or 12 after tumour cell injection. Elongation of early-stage tumours was often observed in the direction in which the needle was inserted during s.c. injection (left). Tumour area calculated in ImageJ is reported beneath each photograph. Scale bars: 10 mm (left) and 5 mm (right). **f**, Trichrome-stained B16 tumour section. Insets depict the cellular (maroon cytoplasm and black nuclei) tumour interior (region 1) and fibrous ECM (blue) and large, round fat droplets (white) at the tumour periphery (region 2). Scale bar: 1 mm. Inset scale bar: 50 μm. **g**,**h**, Ex vivo pipette aspiration rheology of B16 tumours. Brightfield images (**g**-*i*) depict the extension (L) of tumour into the pipette after 90 s of aspiration at the indicated ΔP for an interior tumour region that exhibited large L and required low ΔP (left) and for a peripheral tumour region (fibrotic capsule and adjacent subcutaneous tissue) that exhibited small L and required higher ΔP for measurable deformation (right). Scale bar: 50 μm. Tissue strain L/R_P, where R_P is the radius of the pipette, is plotted (**g**-*ii*) for the constant pressure creep phase (0–90 s) and after the pressure was released back to $\Delta P = 0$ for a representative interior tumour region. The black line depicts non-linear regression of $L(t)/R_P$ to the standard linear solid model, which includes the elastic modulus E as a fitted parameter. Elastic moduli (**h**) fit from the plateau in the strain vs. time plot for interior and peripheral regions of tumours excised days 4, 8, and 12 after engraftment. In the box plot, the centreline depicts the median, the box depicts the IQR, and the whiskers depict the 5th and 95th percentiles. The number of measurements n is combined from two or three tumours per time point. The solid lines are fits of simple exponential growth for the periphery ($E \sim 0.8e^{t/10}$) and exponential decay for the interior ($E \sim 0.5e^{-t/10} + 0.3$), where non-linear regression of the data was constrained so rates and y-intercepts would be shared for the periphery and interior. The shaded box denotes the range of E reported for B16 cells[74,75] that is also typical for B16 tumouroids.

https://doi.org/10.1038/s41551-023-01031-3

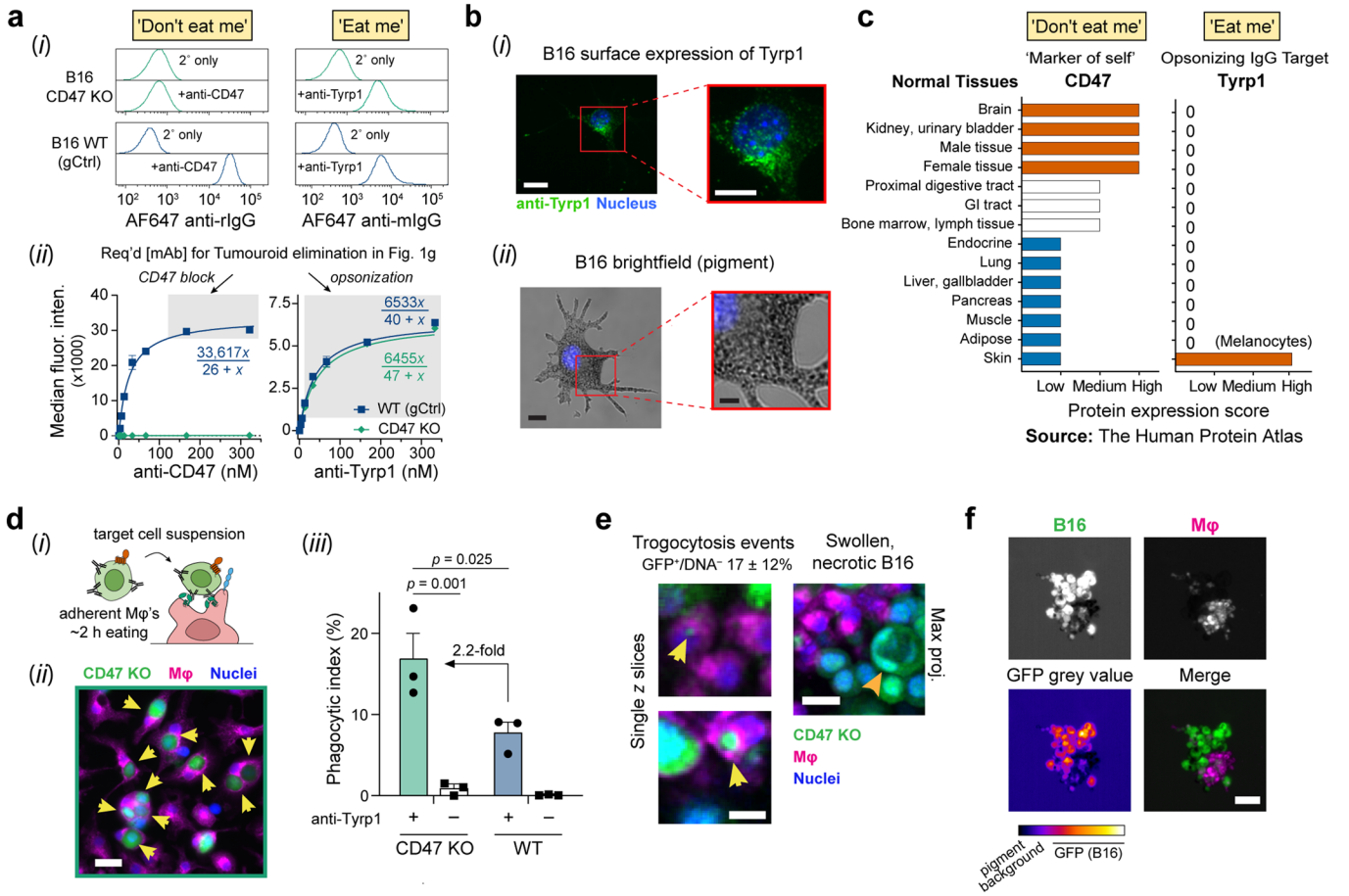

Extended Data Fig. 2 | Analysis of CD47 and Tyrp1 expression and engulfment of B16 tumouroids and cell suspensions. a, Flow cytometry analysis of CD47 and Tyrp1 expression on B16 cell lines. Representative histograms (**a**-*i*) show binding of 10 μg/mL anti-CD47 (left) and 20 μg/mL anti-Tyrp1 (right) to CD47 KO (top) and WT (bottom) B16 cell lines. Binding was detected with secondary antibodies conjugated with Alexa Fluor (AF) 647. The populations shown in the histograms were gated on live, single cells using forward/side scatter and DAPI staining. Median fluorescence intensity (MFI) values (**a**-*ii*) of CD47 KO and WT B16 incubated with varying concentrations of anti-CD47 or anti-Tyrp1 followed by secondary antibody ($n = 3$ tests per antibody concentration, mean ± s.d.). The solid line is a fit of MFI to a hyperbolic model of the form $y = A*x/(K + x)$. The shaded regions correspond to blocking and opsonizing antibody concentrations that are required for tumouroid elimination in Fig. 1g. **b**, Tyrp1 protein expression on B16 melanoma cells. Immunofluorescence image (**b**-*i*) of a B16 cell surface-stained (fixed, unpermeabilized) with anti-Tyrp1 and anti-mouse IgG AF647 (green) and counterstained with Hoechst 33342 (blue). Brightfield image (**b**-*ii*) of a B16 cell. Inset: Pigmented melanosomes. Scale bars: 25 μm (left) and 10 μm (right). **c**, Protein expression data from The Human Protein Atlas[76] for CD47 (https://www.proteinatlas.org/ENSG00000196776-CD47/tissue) and Tyrp1 (https://www.proteinatlas.org/ENSG00000107165-TYRP1/tissue) across different normal tissues. **d**, Conventional 2D phagocytosis (**d**-*i*) of CD47 KO and WT B16 from single-cell suspensions by primary mouse bone marrow-derived macrophages (BMDMs). Representative fluorescence image (**d**-*ii*) of phagocytosis of opsonized CD47 KO (green) by BMDMs (magenta). Yellow arrows denote phagocytic events. Scale bar: 25 μm. The phagocytic index (**d**-*iii*) is calculated as the percentage of macrophages engulfing a target cell multiplied by the number of engulfed cells per macrophage (mean ± s.e.m., $n = 3$ wells per condition). Statistical significance was assessed by two-way ANOVA and Tukey's multiple comparisons test. **e**, Putative tumouroid trogocytic engulfment events consisting of GFP signal without co-localizing DNA signal (yellow arrows) and putative necrotic cell death observed as large, swollen B16 cells in tumouroids (orange arrow). Scale bars: 10 μm (left) and 100 μm (right). **f**, Co-localization of phagocytic macrophages in tumouroids with melanin pigments, which are visualized as a dark shadow in the GFP channel where the signal intensity is below background as illustrated in the colour heat map. Scale bar: 100 μm.

https://doi.org/10.1038/s41551-023-01031-3

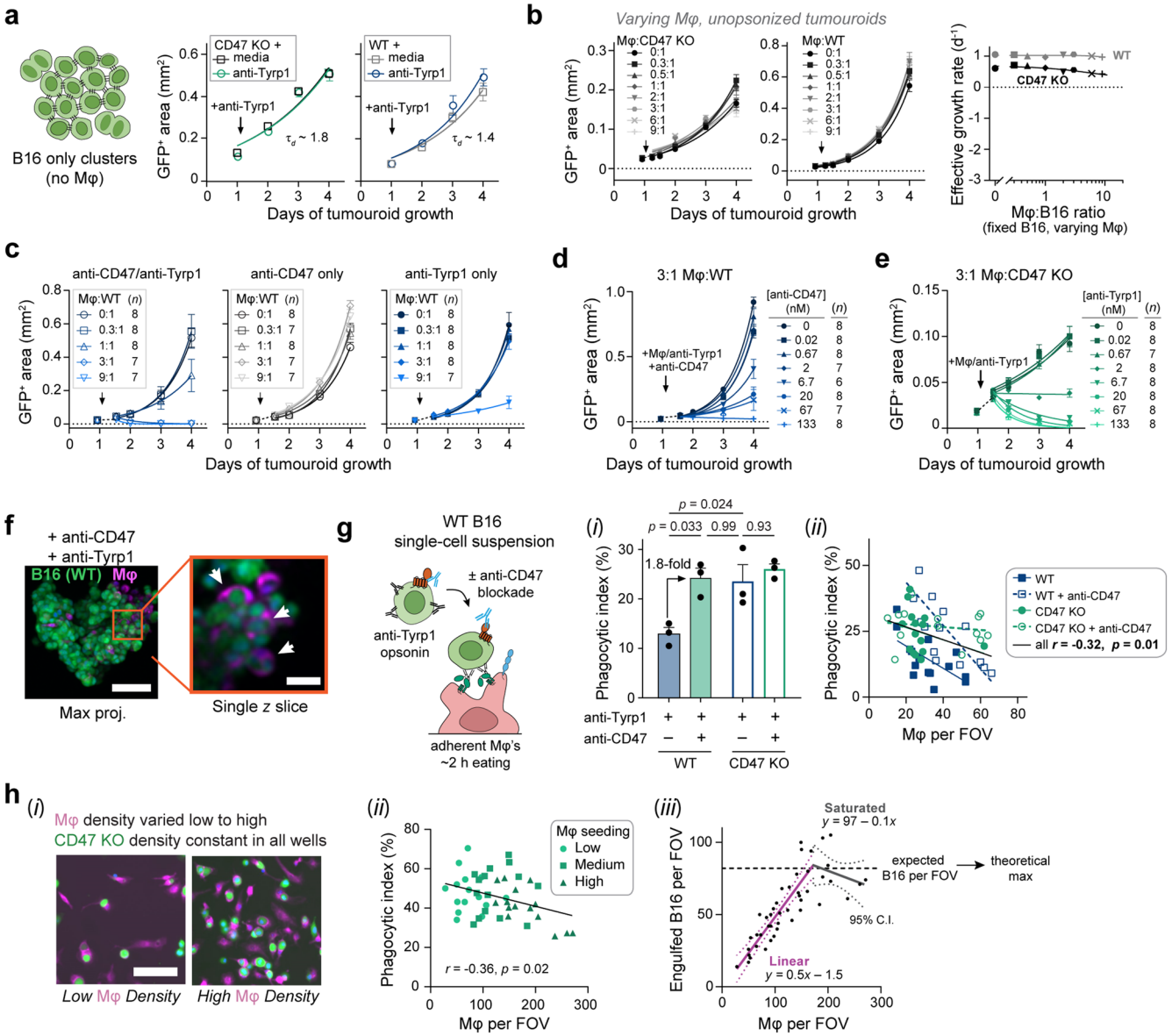

Extended Data Fig. 3 | Cooperative tumouroid phagocytosis and non-cooperative phagocytosis in the conventional 2D assay. a, CD47 KO and WT tumouroid growth curves with or without anti-Tyrp1 added on day 1 in the absence of macrophages (mean ± s.e.m., $n = 6$ tumouroids per condition). **b**, CD47 KO or WT tumouroid growth curves and effective growth rates at varying macrophage:B16 ratios without anti-Tyrp1 (mean ± s.e.m., $n = 8$ tumouroids in a representative experiment). **c**-**e**, Growth curves for WT tumouroids treated with 133 nM anti-CD47 and/or 133 nM anti-Tyrp1 at varying macrophage:WT ratios (**c**), 3:1 macrophage:WT tumouroids with 133 nM anti-Tyrp1 and varying concentrations of anti-CD47 (**d**), and 3:1 macrophage:CD47 KO tumouroids with varying concentrations of anti-Tyrp1 (**e**) (mean ± s.e.m. with exact sample numbers given in the plot legend). The tumouroids in panels (**c**-**e**) correspond to those used to determine k_{eff} as a function of macrophage:WT ratio, anti-CD47 concentration, or anti-Tyrp1 concentration plotted in Fig. 1f, g. **f**, Max intensity projection of confocal images of a WT tumouroid one day after addition of macrophages, anti-Tyrp1, and anti-CD47. Scale bar: 100 µm. The expansion depicts a single z slice with a cluster of macrophages that have engulfed B16 (white arrows). Scale bar: 25 µm. **g**, Phagocytic index for conventional 2D phagocytosis (**g**-*i*) with adherent macrophages and single-cell suspensions of CD47 KO or WT B16 opsonized with anti-Tyrp1 and treated with either anti-CD47 or rat IgG2a isotype control antibody (mean ± s.e.m., $n = 3$ wells per condition). Statistical significance was assessed by two-way ANOVA and Tukey's multiple comparisons test. The phagocytic index (**g**-*ii*) calculated for each field of view (FOV) across all four conditions (2 cell lines x 2 blocking conditions) is plotted against the number of macrophages per FOV (Pearson $r = -0.32$, $p = 0.01$, two-tailed). **h**, Conventional 2D phagocytosis assay with varying macrophage surface densities and a fixed density of CD47 KO B16 opsonized with anti-Tyrp1. Representative FOVs with low and high macrophage density are shown (**h**-*i*). Scale bar: 50 µm. The phagocytic index (**h**-*ii*) calculated for each FOV is plotted against the number of macrophages per FOV as in **g**-*ii* (Pearson $r = -0.36$, $p = 0.02$, two-tailed). Alternatively, the data are fit with a segmental linear regression model (**h**-*iii*) relating the number of engulfed B16 to the number of macrophages per FOV (see Supplementary Fig. 2f for details). The dashed line approximates the expected number of B16 per FOV based on the density of the cell suspension, which is the theoretical maximum number of B16 that can be engulfed even if macrophage density increases.

https://doi.org/10.1038/s41551-023-01031-3

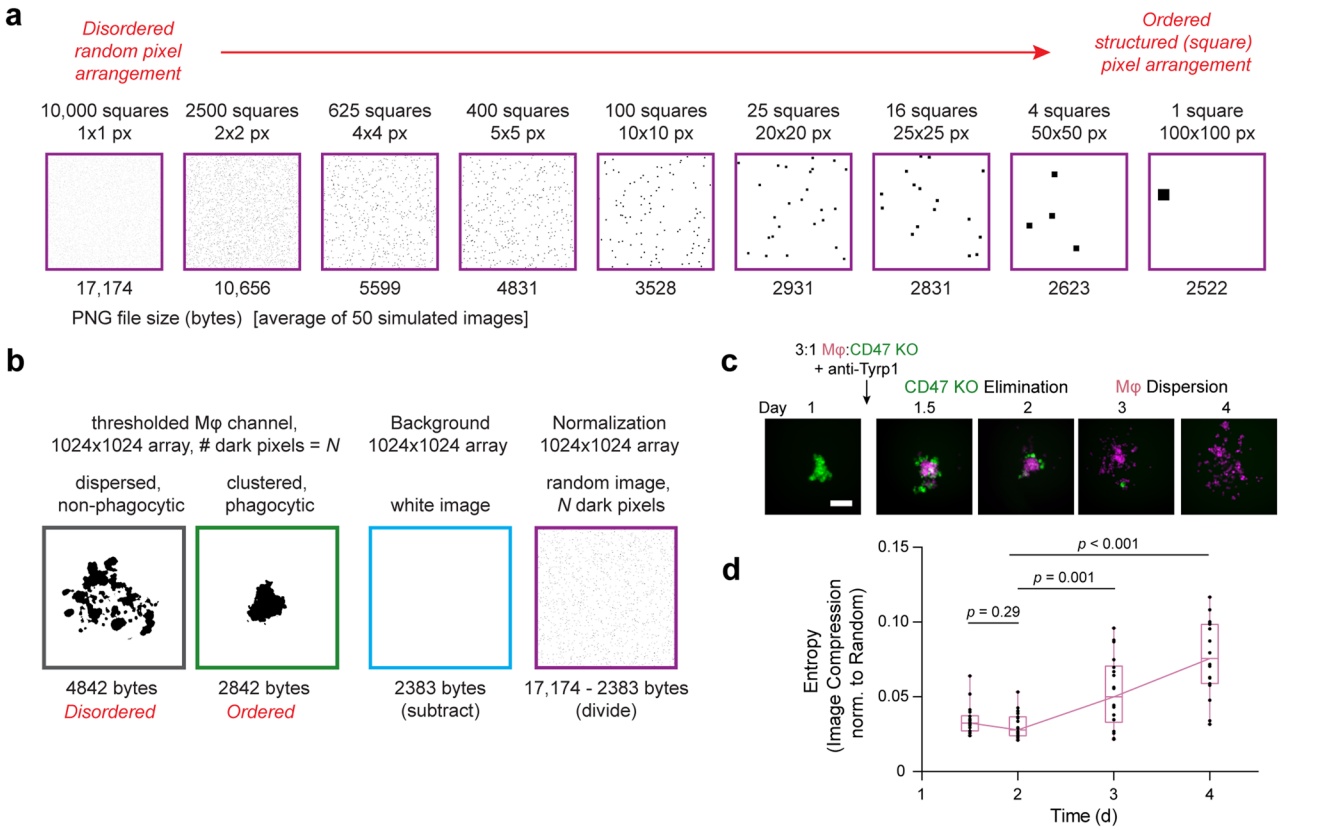

Extended Data Fig. 4 | Informational entropy calculation of macrophage order based on image compression. a, Simulated 1024 × 1024 pixel (px) images containing 10,000 dark px on a white background that are arranged in random squares varying in size from 10,000 1 × 1 px squares to one 100 × 100 px square. The images were compressed in the lossless portable network graphics (PNG) file format. The PNG file size (in bytes) below each image is the average of 50 randomly generated images with the same specifications. **b**, To compare images with different numbers of dark pixels (*N*), a normalization procedure involved subtracting the PNG file size of an equal dimension white image and dividing this value by the PNG file size of an equal dimension random image with *N* dark pixels (minus a white image). **c,d**, Macrophages disperse spontaneously following phagocytosis of tumouroids. Representative images (**c**) of a 3:1 macrophage:CD47 KO tumouroid with anti-Tyrp1 on days 1–4. Scale bar: 100 µm. Macrophage entropy (**d**) during and after elimination of CD47 KO cells from tumouroids. The centreline depicts the median, the box depicts the IQR, and the whiskers depict the range of the data ($n = 18$ tumouroids). Statistical significance was assessed by one-way repeated measures ANOVA followed by Tukey's multiple comparisons test.

https://doi.org/10.1038/s41551-023-01031-3

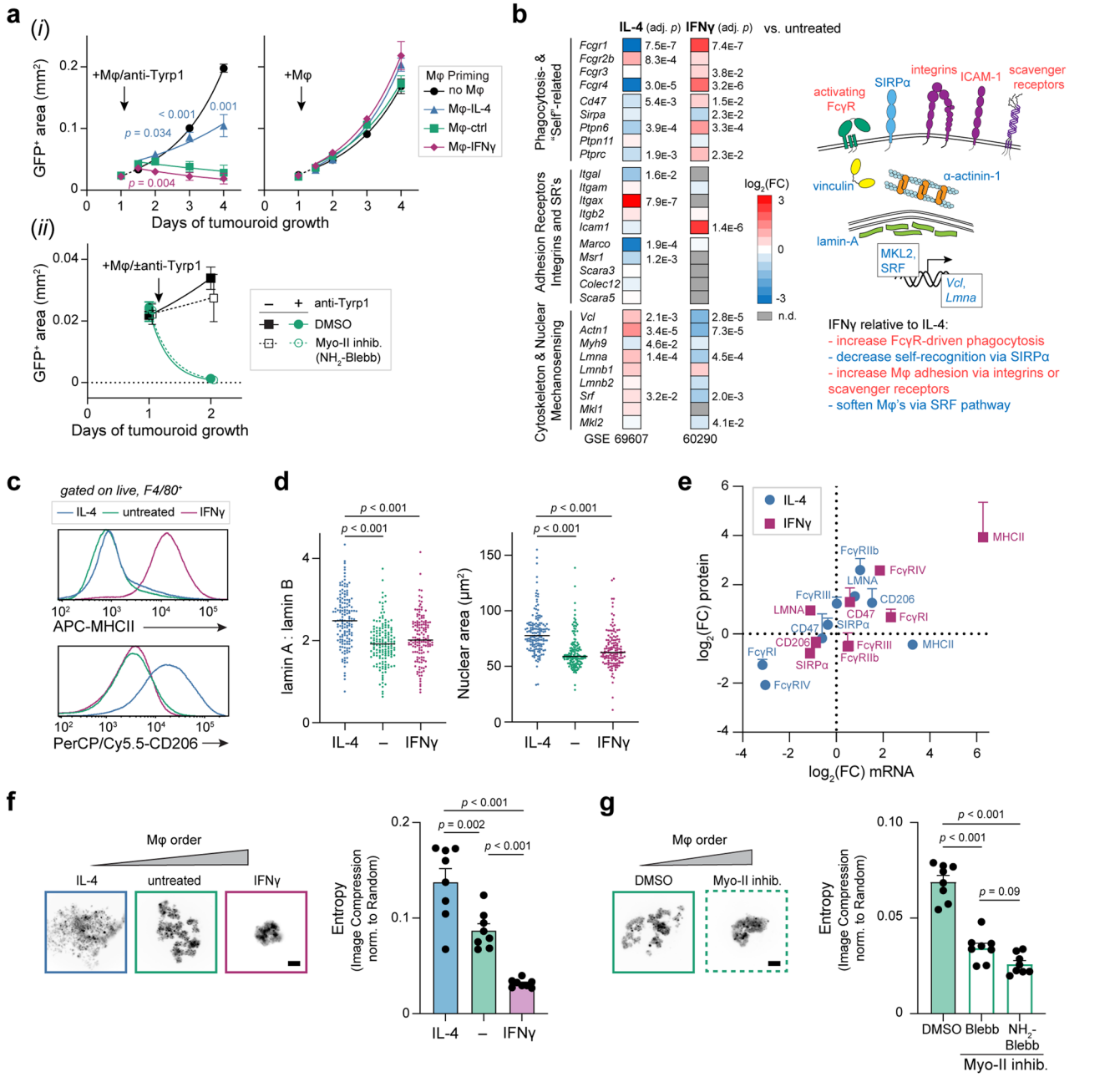

Extended Data Fig. 5 | Effects of cytokine priming or myosin-II inhibition on tumouroid growth suppression and macrophage clustering. **a**, Tumouroid growth curves (**a**-*i*) following addition of macrophages primed for 48 h with 20 ng ml^{-1} IFNγ or 20 ng ml^{-1} IL-4 (mean ± s.e.m, $n = 8$ tumouroids). Statistical significance was assessed by one-way ANOVA and Dunnett's multiple comparisons test between the mean area of tumouroids with unprimed macrophages and tumouroids with cytokine-primed macrophages at each time point. Growth curves for CD47 KO tumouroids (**a**-*ii*) in the presence of 20 μM *p*-amino-blebbistatin (NH_2-blebb) to inhibit myosin-II or DMSO vehicle control (mean ± s.e.m., $n = 4$ tumouroids). **b**, Transcriptomic microarray analyses of BMDMs treated with IFNγ (GSE60290) (ref. 70) or IL-4 (GSE69607) (ref. 71) versus untreated BMDMs. The *p* values for differentially expressed genes were adjusted for multiple comparisons by the method of Benjamini and Hochberg to control the false discovery rate. The heat map depicts $\log_2$(fold change) for selected genes. Proteins encoded by differentially expressed genes are depicted in the schematic detailing a putative cytoskeleton and nuclear mechanosensing pathway and membrane receptors involved in phagocytosis and macrophage adhesion. **c**-**e**, Measurements of protein expression of selected differentially expressed genes in BMDMs treated with IFNγ or IL-4 for 48 h. Flow cytometry histograms (**c**) for surface staining of MHCII and CD206 in IFNγ- or IL-4-treated or untreated BMDMs. Similar staining was performed with antibodies against FcR's, CD47, and SIRPα. The ratio of lamin-A to lamin-B and the projected nuclear area were quantified (**d**) by immunofluorescence microscopy (individual values for $n > 140$ cells per condition across 8 fields of view with a line denoting the median). Statistical significance was assessed by one-way ANOVA followed by Tukey's multiple comparisons test. Scatterplot (**e**) of the fold change (cytokine-primed vs. untreated) of indicated proteins from flow cytometry (panel **c**) (mean ± s.d., replicates were BMDMs from $n = 3$ mice for MHCII staining and 4 mice for all other proteins) and lamin-A immunofluorescence staining (panel **d**) versus the fold change in gene expression from microarrays (panel **b**). **f**,**g**, Representative fluorescence images and entropy analysis for cytokine-primed (**f**) and blebbistatin-treated (**g**) macrophage monocultures on non-adhesive surfaces (mean ± s.e.m, $n = 8$ wells per condition). Cytokines and drugs were added after 6 h and images were acquired 20 h later. Scale bars: 100 μm. Statistical significance in panels **f**,**g** was assessed by one-way ANOVA followed by Tukey's multiple comparisons test.

https://doi.org/10.1038/s41551-023-01031-3

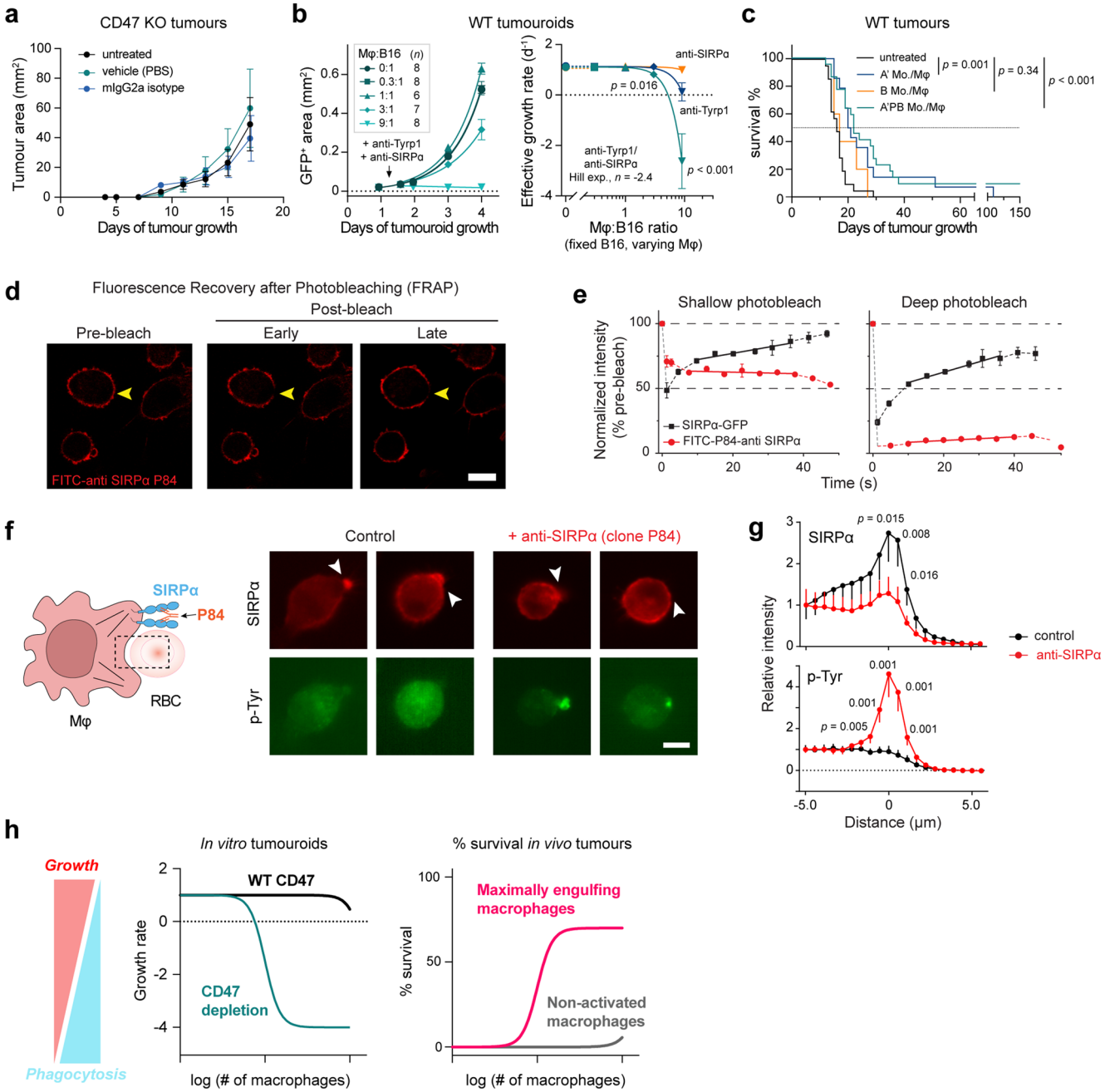

Extended Data Fig. 6 | Isotype control, vehicle injections, and FcR-primed, SIRPα-blocked marrow cell injections; Biophysical crosslinking mechanism for SIRPα blockade by the anti-mouse SIRPα mAb clone P84. a, Growth curves of tumours in mice injected with 2×10^5 CD47 KO cells and treated i.v. on days 4, 5, 7, 9, 11, 13, and 15 with 250 μg mouse IgG2a isotype control, with PBS vehicle, or left untreated (mean ± s.e.m., $n = 6$ mice per group). **b**, WT tumouroid growth curves and effective growth rates at varying macrophage:B16 ratios with anti-Tyrp1 and/or anti-SIRPα (mean ± s.e.m., $n = 6$–8 tumouroids in a representative experiment with exact n for anti-SIRPα + anti-Tyrp1 tumouroids reported in the plot legend). Statistical significance was assessed at each macrophage:B16 ratio by one-way ANOVA and Tukey's multiple comparisons test. The p values reported in the plot correspond to differences in mean area between tumouroids treated with anti-SIRPα + anti-Tyrp1 and with anti-Tyrp1 only. **c**, Survival curves of mice bearing WT B16 tumours (parental line) treated with 2×10^7 A'PB ($n = 22$ mice), A' (FcR-primed only, no SIRPα block; $n = 14$), or B (no FcR priming, only SIRPα block; $n = 5$) marrow cells i.v. on day 4 after tumour engraftment or left untreated ($n = 21$ mice). A'PB and A' conditions included additional 250 μg anti-Tyrp1 i.v. on days 5, 7, 9, 11, 13, and 15. Statistical significance was determined by the log-rank (Mantel-Cox) test. **d-g**, Anti-mouse SIRPα antibody clone P84 binds to mouse macrophages and immobilizes SIRPα. Representative fluorescence images (**d**) and quantification (**e**) of fluorescence recovery after photobleaching (FRAP) for SIRPα-GFP ± anti-mSIRPα clone P84. Bleached regions (yellow arrow) are shown prior to bleaching and at early and late time points of recovery ($n = 3$). Scale bar: 10 μm. Experimental schematic and representative images (**f**) of J774A.1 mouse macrophages ± anti-mSIRPα clone P84 incubated with IgG-opsonized mouse RBCs for 30 min prior to immunostaining for SIRPα and phospho-tyrosine (p-Tyr). Quantification (**g**) of SIRPα and p-Tyr immunofluorescence at the phagocytic synapse between the macrophage and target RBC. Scale bar: 10 μm. Fluorescence intensity in the phagocytic synapse was normalized to fluorescence from macrophages that were not undergoing phagocytosis (mean ± s.e.m., $n = 7$). Statistical significance of each imaging bin along the phagocytic synapse was assessed by Welch's t-test (two-tailed, unpaired with Holm-Šídák correction for multiple comparisons). **h**, Summary of macrophage number versus therapeutic outcome for tumouroids in vitro and tumours in vivo. Growth rate is controlled by tumour cell proliferation and macrophage phagocytosis. CD47 signalling dominates pro-phagocytic signalling at low and high macrophage numbers, but CD47 depletion, IgG opsonization, and macrophage infiltration can eliminate tumours.

https://doi.org/10.1038/s41551-023-01031-3

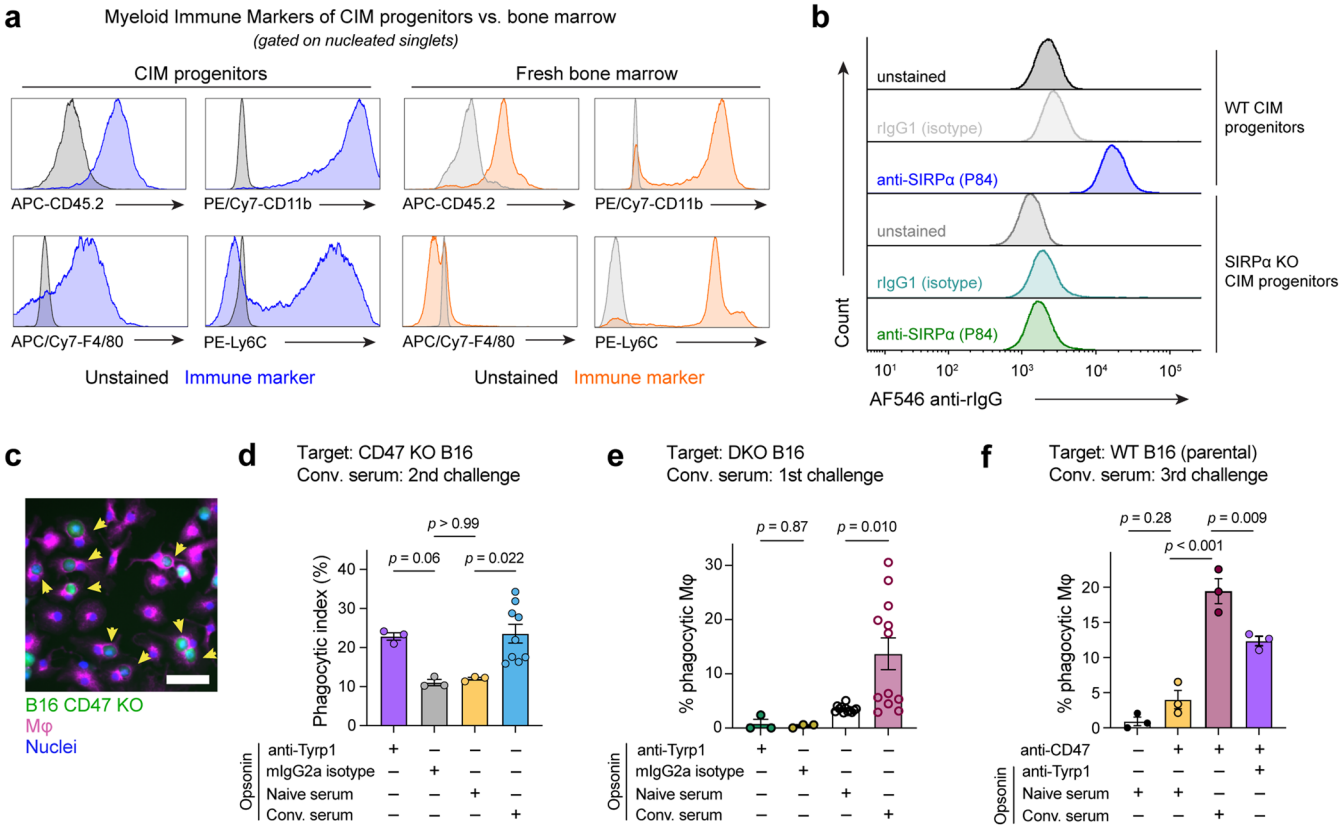

Extended Data Fig. 7 | Conditionally immortalized macrophage progenitor engineering and opsonization of various B16 lines with convalescent serum. **a**,**b**, Flow cytometry analysis of surface markers on conditionally immortalized macrophage (CIM) progenitors. Staining for myeloid markers (**a**) on CIM progenitors and freshly harvested bone marrow cells for comparison. Flow histograms of SIRPα staining (**b**) on SIRPα KO CIM progenitors and unedited wild-type CIM progenitors. Anti-SIRPα binding was detected with AF546 anti-rat IgG. **c**–**f**, Convalescent serum IgG from CD47 KO tumour complete responders opsonizes CD47 KO, DKO, and WT B16. (**c**) Representative fluorescence image of serum-opsonized CD47 KO B16 engulfed by BMDMs (yellow arrows). Scale bar: 50 µm. (**d**) Quantification of the phagocytic index for macrophages engulfing CD47 KO B16 opsonized with convalescent sera, naïve serum, or mAb controls. Convalescent sera were collected from second challenge survivors 70 days after tumour challenge (mean ± s.e.m., $n = 3$ wells for antibody conditions, $n = 3$ wells per serum sample for one naïve serum and three convalescent sera). (**e**) Percent phagocytic macrophages engulfing DKO B16 (lacking CD47 and Tyrp1) opsonized with convalescent sera collected from first challenge survivors 99 days after tumour challenge, naïve sera, or mAb controls (mean ± s.e.m., $n = 3$ wells for antibody conditions, $n = 3$ wells per serum sample for four naïve or convalescent sera). (**f**) Percent phagocytic macrophages engulfing WT B16 opsonized with convalescent serum from a third challenge survivor, naïve serum, or anti-Tyrp1 (mean ± s.e.m., $n = 3$ wells per condition). In panels (d-f), statistical significance was assessed by one-way ANOVA and Šídák's multiple comparisons test between selected groups.

https://doi.org/10.1038/s41551-023-01031-3

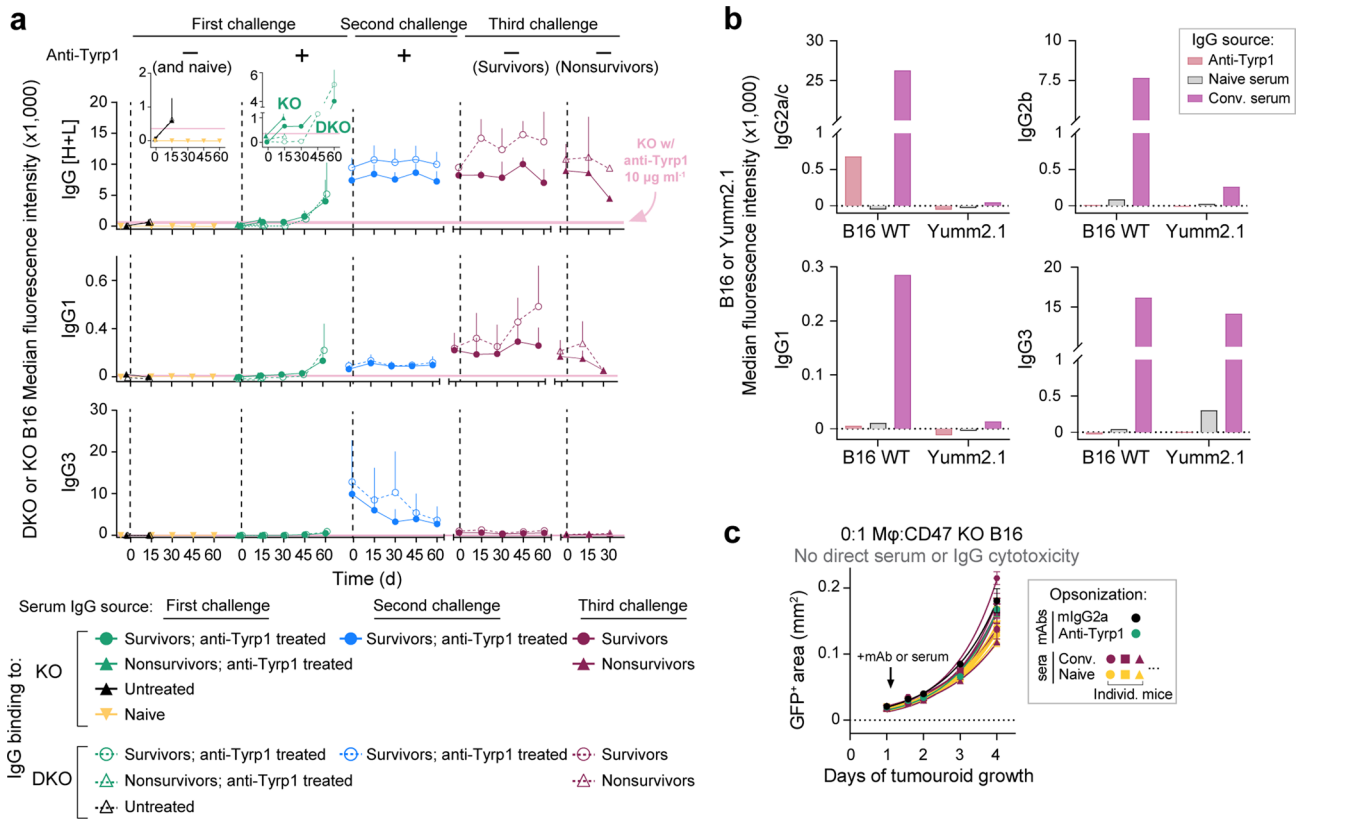

Extended Data Fig. 8 | Convalescent sera from CD47 KO tumour complete responders contain multiple subclasses of IgG that bind CD47 KO and DKO B16, but not syngeneic YUMM2.1 melanoma cells. a, Kinetics of de novo IgG generation revealed by flow cytometry of CD47 KO (filled symbols) and DKO B16 cells (open symbols) stained with serum followed by a polyclonal anti-mouse IgG [H+L] secondary antibody (row 1) or secondary antibodies specific for mouse IgG1 and IgG3 (rows 2 and 3). The corresponding data for IgG2a/c and IgG2b are shown in Fig. 6b. The median fluorescence intensity was corrected by subtracting the background fluorescence equal to the signal of cells incubated with secondary antibodies only. Symbols and error bars depict the mean ± s.e.m. of each group. The range of staining observed with 10 μg ml^{-1} anti-Tyrp1 is denoted by the pink boxes or lines. The gating strategy and representative histograms are shown in Supplementary Fig. 4. **b**, Median fluorescence intensity of B16 WT or Yumm2.1 cells incubated with 5% (v/v) serum collected from a mouse that survived the third challenge, with naïve serum, or with anti-Tyrp1 followed by staining with monoclonal secondary antibodies as in Fig. 6b and panel (a) of this figure. **c**, Growth curves for CD47 KO tumouroids treated with convalescent serum, naïve serum, anti-Tyrp1, or mIgG2a isotype control Ab without macrophages. Solid lines are non-linear regression of the data to a simple exponential of the form $A(t) = A_1 e^{k(t-1)}$ (mean ± s.e.m., $n = 3$ or 4 tumouroids each for anti-Tyrp1, mIgG2a, 9 convalescent sera, and 9 naïve sera).

https://doi.org/10.1038/s41551-023-01031-3

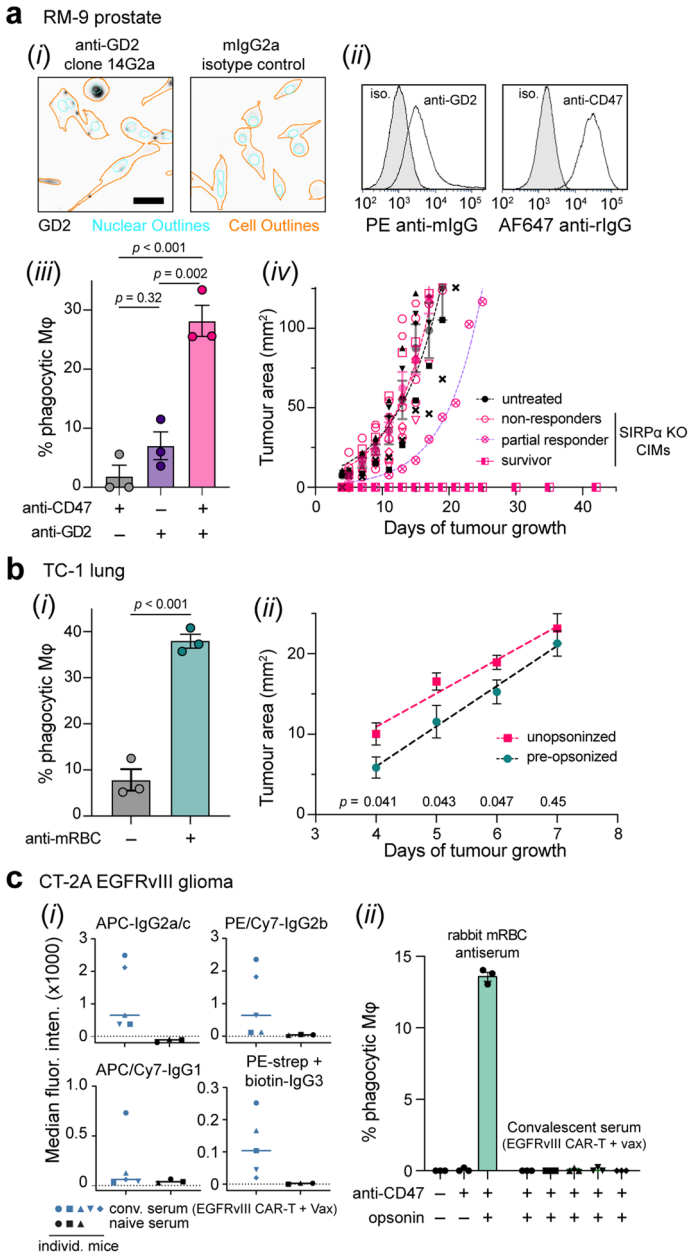

Extended Data Fig. 9 | See next page for caption.

https://doi.org/10.1038/s41551-023-01031-3

Extended Data Fig. 9 | Generalization of CD47 disruption and macrophage phagocytosis in prostate, lung, and glioblastoma tumour models. a, Targeting RM-9 prostate tumours for phagocytosis. Immunostaining of RM-9 (**a**-*i*) with anti-GD2 and mIgG2a isotype control Ab. Bound primary antibodies were detected with a secondary antibody conjugated with AF647. Clusters of anti-GD2 are consistent with 'cap formation' as should occur due to GD2 association with rafts[77] or due to the polyclonal secondary antibody. Scale bar: 100 µm. Flow cytometry histograms (**a**-*ii*) of anti-GD2 (left) and anti-CD47 (right) and their isotype (iso.) controls binding to RM-9. Bound primary antibodies were detected with secondary antibodies conjugated with PE and AF647, respectively. Phagocytosis of RM-9 cells (**a**-*iii*) by BMDMs with anti-GD2 opsonization and/or CD47 antibody blockade. Statistical significance was assessed by one-way ANOVA with Tukey's multiple comparisons test (mean ± s.e.m., $n = 3$ wells per condition). WT RM-9 tumour growth curves (**a**-*iv*). Mice were treated with 4×10^6 SIRPα KO CIM progenitors i.v. on day 4 and 250 µg anti-GD2 i.v. on days 4, 5, 7, 9, 11, 13, and 15 ($n = 10$) or left untreated ($n = 5$). Each symbol represents a separate tumour, and complete responses ('survivor', 1) in which a tumour was never palpable are depicted with the half-filled squares. **b**, Targeting TC-1 lung tumours for phagocytosis. (**b**-*i*) Phagocytosis of CD47 KO TC-1 by BMDMs with anti-mouse RBC IgG opsonization (mean ± s.e.m., $n = 3$ per condition). Statistical significance was assessed by Welch's *t*-test (two-tailed, unpaired). (**b**-*ii*) Tumour growth curves at early timepoints following injection of TC-1 cells pre-opsonized with anti-mouse RBC and anti-CD47 or unopsonized controls (mean ± s.e.m., $n = 10$ mice per group). Statistical significance at each timepoint between control (squares) and pre-opsonized (circles) was assessed by Student's *t*-test (two-tailed, unpaired). The dashed lines are linear fits, which were compared by the extra sum-of-squares *F* test ($p = 0.002$, two-tailed). **c**, Binding and functional analysis of convalescent serum IgG from vaccine-enhanced CAR-T therapy against CT-2A glioma[54]. Median fluorescence intensity (**c**-*i*) (corrected by subtracting the background signal measured on unstained cells) of CT-2A stained with 5% (v/v) convalescent or naïve serum followed by the same secondary Ab panel used for Fig. 6b and Extended Data Fig. 8a, b (median with all data points, $n = 5$ convalescent and 3 naïve sera). (**c**-*ii*) Lack of phagocytosis of CT-2A cells treated with convalescent sera even when CD47 was blocked. As a positive control, CT-2A were opsonized with 5% (v/v) anti-mRBC polyclonal antiserum (mean ± s.d., $n = 3$ wells per condition).

https://doi.org/10.1038/s41551-023-01031-3

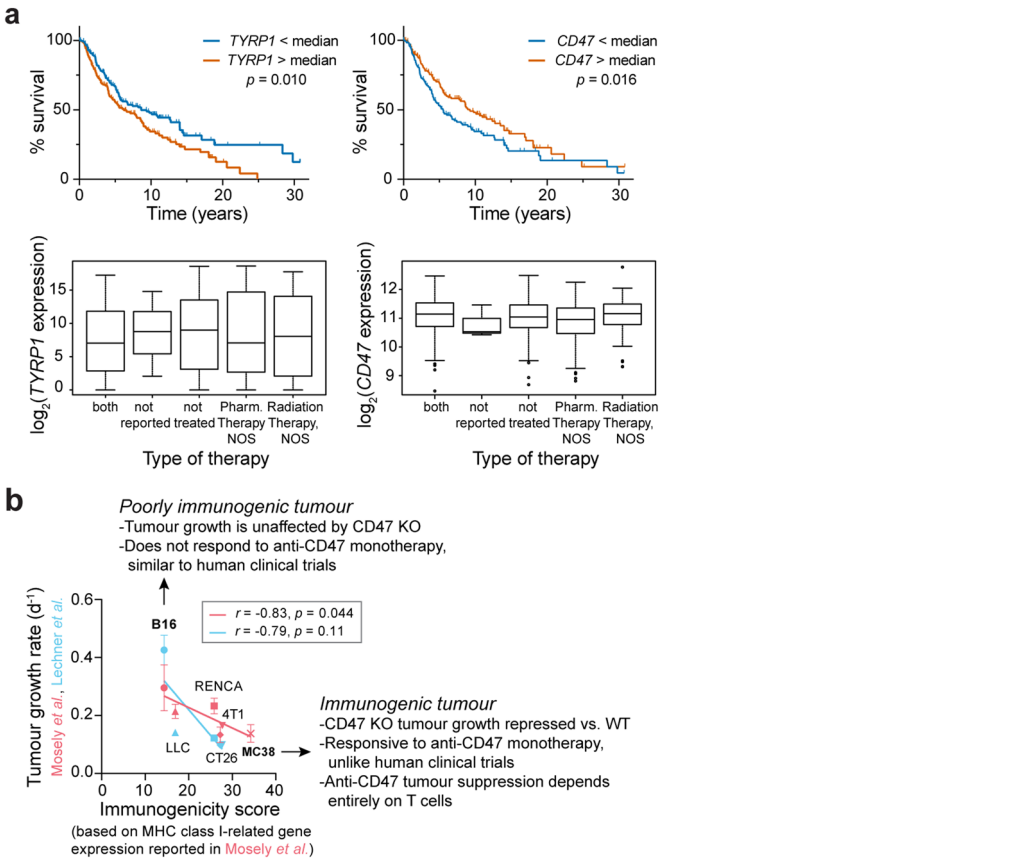

Extended Data Fig. 10 | Potential for combination immunotherapy in human melanoma and rationale for CD47 combination therapy versus monotherapy in syngeneic mouse models. a, TCGA analysis of *TYRP1* and *CD47* in human melanoma. Survival analysis of metastatic melanoma patients in The Cancer Genome Atlas (TCGA SKCM) based on expression of *TYRP1* (left) and *CD47* (right) above or below the median. Significance was determined by the log-rank (Mantel-Cox) test. Expression levels of *TYRP1* (left, one-way ANOVA, $p = 0.68$) and *CD47* (right, $p = 0.36$) across different treatment modalities reported in TCGA. In the box plots, the centreline depicts the median, the boxes span the IQR, and the whiskers span 1.5 × IQR with outlier points included. **b**, Meta-analysis of tumour growth from data reported by Mosely *et al.*[78] and Lechner *et al.*[79] across different syngeneic mouse tumour models plotted against an immunogenicity score defined as the summation of $\log_2$(expression) of MHC class I-related genes reported by Mosely *et al.* (Pearson correlation coefficients *r* and two-tailed *p* values are reported in the plot legend). Graphical growth data were digitized using WebPlotDigitizer version 4.2, and growth curves were fit to the exponential growth equation $V(t) = V_0 e^{kt}$ to determine the tumour growth rate *k* (± standard error). Tumour types are: melanoma (B16), lung (LLC), kidney (RENCA), breast (4T1), and colon (CT26 and MC38). Note that B16 doubling rates in our studies are consistent with the data here, even with CD47 knockout.

nature portfolio

Corresponding author(s): Dennis E. Discher

Last updated by author(s): Mar 23, 2023

Reporting Summary

Nature Portfolio wishes to improve the reproducibility of the work that we publish. This form provides structure for consistency and transparency in reporting. For further information on Nature Portfolio policies, see our Editorial Policies and the Editorial Policy Checklist.

Statistics

For all statistical analyses, confirm that the following items are present in the figure legend, table legend, main text, or Methods section.

n/a	Confirmed	
☐	☒	The exact sample size (*n*) for each experimental group/condition, given as a discrete number and unit of measurement
☐	☒	A statement on whether measurements were taken from distinct samples or whether the same sample was measured repeatedly
☐	☒	The statistical test(s) used AND whether they are one- or two-sided *Only common tests should be described solely by name; describe more complex techniques in the Methods section.*
☒	☐	A description of all covariates tested
☐	☒	A description of any assumptions or corrections, such as tests of normality and adjustment for multiple comparisons
☐	☒	A full description of the statistical parameters including central tendency (e.g. means) or other basic estimates (e.g. regression coefficient) AND variation (e.g. standard deviation) or associated estimates of uncertainty (e.g. confidence intervals)
☐	☒	For null hypothesis testing, the test statistic (e.g. *F*, *t*, *r*) with confidence intervals, effect sizes, degrees of freedom and *P* value noted *Give P values as exact values whenever suitable.*
☒	☐	For Bayesian analysis, information on the choice of priors and Markov chain Monte Carlo settings
☒	☐	For hierarchical and complex designs, identification of the appropriate level for tests and full reporting of outcomes
☐	☒	Estimates of effect sizes (e.g. Cohen's *d*, Pearson's *r*), indicating how they were calculated

Our web collection on statistics for biologists contains articles on many of the points above.

Software and code

Policy information about availability of computer code

Data collection	BD Diva, Micro-Manager, Leica LAS X, LiCor Odyssey Application Software, Validyne USB-COM Data Logger
Data analysis	FCS Express 7 Research Edition, GraphPad Prism v8-9, Microsoft Excel, ImageJ/FIJI (Bio-Formats, Radial Profile plugins), GEO2R Webtool, Python 3 with Numpy and PIL/Pillow packages, WebPlot Digitizer version 4.2

For manuscripts utilizing custom algorithms or software that are central to the research but not yet described in published literature, software must be made available to editors and reviewers. We strongly encourage code deposition in a community repository (e.g. GitHub). See the Nature Portfolio guidelines for submitting code & software for further information.

Data

Policy information about availability of data

All manuscripts must include a data availability statement. This statement should provide the following information, where applicable:

- Accession codes, unique identifiers, or web links for publicly available datasets
- A description of any restrictions on data availability
- For clinical datasets or third party data, please ensure that the statement adheres to our policy

The main data supporting the results in the study are available within the paper and its Supplementary Information. Source data for the tumour-growth curves in Figs. 3f and 6c and in Extended Data Figs. 6a and 9a,b are provided with this paper. No large sequencing datasets were generated as part of this study, yet publicly available data from The Cancer Genome Atlas, The Human Protein Atlas, and the NCBI GEO Repository were accessed via the identifiers provided in Methods and in the relevant figure captions.

Field-specific reporting

Please select the one below that is the best fit for your research. If you are not sure, read the appropriate sections before making your selection.

☒ Life sciences ☐ Behavioural & social sciences ☐ Ecological, evolutionary & environmental sciences

For a reference copy of the document with all sections, see nature.com/documents/nr-reporting-summary-flat.pdf

Life sciences study design

All studies must disclose on these points even when the disclosure is negative.

Sample size	Sample-size calculations were not performed a priori. Sample sizes in each experiment were chosen for practical considerations (such as injecting cell suspensions while cells remained viable).
Data exclusions	Images were excluded from analyses if debris obstructed accurate measurement or interfered with cell growth. Outlier analysis for growth rates in tumouroid studies was performed in Graphpad Prism using the ROUT method (Q = 1%). At most, one outlier was removed from samples of 7 or 8 tumouroids.
Replication	The results were reproducible and in most cases replicated by multiple researchers.
Randomization	We allocated mice randomly using a random number generator to sort mice into treatment groups.
Blinding	When possible, given practical considerations, mouse experiments included blinding of the researcher performing tumour inoculations and treatments and of the researcher measuring tumor growth. Some in vitro assays analysing phagocytosis also included blinding wherein the researcher performing and analysing the experiment did not know the identity of the samples until the analysis was complete.

Reporting for specific materials, systems and methods

We require information from authors about some types of materials, experimental systems and methods used in many studies. Here, indicate whether each material, system or method listed is relevant to your study. If you are not sure if a list item applies to your research, read the appropriate section before selecting a response.

Materials & experimental systems

n/a	Involved in the study
☐	☒ Antibodies
☐	☒ Eukaryotic cell lines
☒	☐ Palaeontology and archaeology
☐	☒ Animals and other organisms
☒	☐ Human research participants
☒	☐ Clinical data
☒	☐ Dual use research of concern

Methods

n/a	Involved in the study
☒	☐ ChIP-seq
☐	☒ Flow cytometry
☒	☐ MRI-based neuroimaging

Antibodies

Antibodies used	Details, including clone names for monoclonal antibodies, suppliers, catalogue numbers, lot numbers, conjugations where applicable, and concentrations or dilutions, are detailed in Supplementary Tables 1–3.
Validation	The binding of antibodies used in phagocytosis assays for opsonization or CD47/SIRPalpha blockade was confirmed on relevant cell types by flow cytometry and/or immunofluorescence staining (as in Extended Data Figs. 2a,b, 6d–g and 9a). Otherwise, experiments conformed to the recommended applications listed by the antibody suppliers.

Eukaryotic cell lines

Policy information about cell lines

Cell line source(s)	B16-F10 were obtained from ATCC (CRL-6475), and engineered versions are described in this paper and/or in Hayes et al. JCS 2020 (ref. 66). YUMM2.1 cells were a gift from Dr. Chi Van Dang. The original derivation of the cell line is described in ref. 48. TC-1 cells were a gift from Dr. Sunil Singhal. The original derivation of the cell line is described in ref. 52. CT-2A EGFRvIII cells were engineered, as described in Ma et al. Science, 2019 (ref. 54). RM-9 cells were obtained from ATCC (CRL-3312). J774A.1 cells were obtained from ATCC (TIB-67).

	Conditionally immortalized macrophage (CIM) progenitors were a gift from Dr. Igor Brodsky. The original derivation of CIMs is described in ref. 45 and the derivation of Cas9+ CIMs in ref. 46.
Authentication	B16-F10 produced melanin pigment consistent with melanoma and surface stains with Tyrp1, as reported by Takechi et., Clinical Cancer Research 1996 (PMID: 9816138). Other cell lines were not additionally authenticated.
Mycoplasma contamination	Cell lines were not routinely tested for mycoplasma.
Commonly misidentified lines (See ICLAC register)	The cell lines used in this study are not found on version 11 of the ICLAC register.

Animals and other organisms

Policy information about studies involving animals; ARRIVE guidelines recommended for reporting animal research

Laboratory animals	Male and female C57BL/6J mice were acquired from Jackson labs (> 6 weeks old; 6–12-week-old mice were used for first challenge experiments, and aged mice up to 52 weeks were procured for age-matched controls). Male NSG (NOD scid gamma) mice were bred at the Stem Cell Xenograft Core at the University of Pennsylvania (6–10 weeks old).
Wild animals	The study did not involve wild animals.
Field-collected samples	The study did not involve samples collected from the field.
Ethics oversight	All experiments were performed in accordance with protocols approved by the Institutional Animal Care and Use Committee of the University of Pennsylvania (IACUC protocols 804455 and 803177).

Note that full information on the approval of the study protocol must also be provided in the manuscript.

Flow Cytometry

Plots

Confirm that:

☒ The axis labels state the marker and fluorochrome used (e.g. CD4-FITC).

☒ The axis scales are clearly visible. Include numbers along axes only for bottom left plot of group (a 'group' is an analysis of identical markers).

☒ All plots are contour plots with outliers or pseudocolor plots.

☒ A numerical value for number of cells or percentage (with statistics) is provided.

Methodology

Sample preparation	Cell lines and primary mouse macrophages differentiated in culture were detached from flasks or dishes and counted prior to staining. Tumour tissues were minced with a razor plate or scalpel and disaggregated enzymatically by Dispase and collagenase at 37 °C. Single-cell suspensions in FACS buffer [PBS + 1% (w/v) bovine serum albumin or 2% (v/v) fetal bovine serum + 0.1% (w/v) sodium azide] were stained on ice or on a tube rotator located in a 4 C cold room. Cells were washed 3x in FACS buffer to remove unbound Ab's by centrifugation at 300–500g for 3–5 min. Final re-suspensions were in 500 µL FACS buffer with 0.2 µg/mL DAPI if cells were to be analysed immediately. Otherwise, cells were stained with Zombie aqua fixable cell viability dye prior to Ab staining. Cells were fixed in formaldehyde solutions as described in Methods and stored at 4 °C until analysis (within a week).
Instrument	BD LSRII, maintained by the Penn Cytomics and Cell Sorting Resource Laboratory (instruments A and B).
Software	FCS Express 7 Research Edition
Cell population abundance	No post-sorted fractions were generated.
Gating strategy	Events were gated on FSC-H vs FSC-A (and SSC-H vs SSC-A) for singlet vs. doublet discrimination. Cell events were gated from debris events based on SSC-A vs. FSC-A. Further gating for live cells was performed with DAPI or Zombie aqua, or for nucleated events with Hoechst. Examples are provided in the Supplementary Information. Gates for the positive expression of a marker or dye label were set based on unstained or isotype-control-stained samples.

☒ Tick this box to confirm that a figure exemplifying the gating strategy is provided in the Supplementary Information.